



Universitat
Rostock



Fakultat fur Informatik



SOLENT
UNIVERSITY
SOUTHAMPTON



Zachodniopomorski
Uniwersytet
Techniczny
w Szczecinie



Prediction of Ship Maneuverability

Submitted on 24 August 2020

by

NATH ADWAITH
5 Rue des Renards, 44072 Nantes
Student Id: S182732
adwaith.nath@gmail.com

Supervisor: Patrick QUEUTEY
Associate Supervisor: Ganbo DENG

First Reviewer:

Prof. Felicien BONNEFOY
Professor (ECN)
Nantes, 44000

Second Reviewer:

Prof. David LE TOUZE
Professor (ECN)
Nantes, 44000



This Master Thesis has been prepared as part of the graduation of the Master in Marine Technology specialized in Hydrodynamics for Ocean Engineering from Centrale Nantes and the graduation of the double Master degree Liege University-Centrale Nantes in the EMship+ programme

ABSTRACT

With the ever increasing marine traffic, the concerns over ship's ability to avoid collisions have gained much importance in recent year. Due to the complex nature of flow associated with the maneuvers, CFD has been used as a tool either in calculating the hydrodynamics derivatives for mathematical model or have been directly the flow. To have a better understanding of the complex flow during such maneuvers, this study is dedicated to the latter case to directly solve the flow using CFD.

This work studies the blind test case for SIMMAN 2020 workshop on the deep water turning circle maneuver of the KCS hull with modelled propeller and rudder. The propeller thrust are simulated in two different methods: Rotating frame / Static rotor method and the Resolved propeller. The simulation of the 35 deg starboard turning circle is carried out in two stages. The first stage involves a 3-dof simulation to predict of the rps of the propeller to maintain the speed corresponding to $FrNo = 0.26$ and the next stage involves the 6-dof turning circle with the imposed rps.

The ISIS-CFD solver developed by the METHRIC team has been used for this study. A novel method of adaptive grid refinement implemented in the solver for refinement of free surface and inter-grid boundaries have been utilized and discussed in this study. A novel method called adaptive grid refinement has been utilized to refine the free surface and domain boundaries as teh simulation progresses. The results from the simulations are validated against EFD data from MARIN(for turning circle) and IIHR (for self propulsion). A detailed assessment of the forces, moments and vortical structures involved in the turning circle has been discussed.

ACKNOWLEDGEMENTS

At the end of this journey, I would like to express my sincere thanks to people whose help were instrumental in completion of this work.

Firstly, I would like to express my deepest appreciation to my supervisor, Dr. Patrick Queutey, for giving me the opportunity to work with the METHRIC team, LHEEA. His valuable advice, knowledge, support and profound belief in my abilities played a key role in the realization of this work. I am also extremely grateful to my co-Supervisor, Dr. Ganbo Deng, for his guidance and invaluable insight on overset interpolation. I also wish to thank Dr. Jeroen Wackers for sharing his knowledge on Adaptive grid refinement. I would like to thank Ms. Ginevra Rubino of the METHRIC team for her help and advice on assessing and documenting the results of this work.

The computational resources required for the simulations conducted in this work were exorbitant. I would like to extend my deepest gratitude to LHEEA and CNRS for the generous time granted on the LIGER HPC cluster.

This project forms a part of the EMSHIP master's program and so I would like to thank the the coordinator of the program, Dr. Rigo Philippe from University of Liege, and coordinator form Ecole Central de Nantes, Dr. Lionel Gentaz for their unwavering support throughout the course.

I would like to thank my mother and father, who are the two pillars in my life, and Ms. Madhushri Varunjikar for their unwavering love and support. Last but not the least, I would like to thank my friends for their moral support and encouragement.

Contents

ABSTRACT	ii
ACKNOWLEDGEMENTS	iii
CONTENTS	iv
List of Figures	vi
DECLARATION OF AUTHORSHIP	viii
Chapter 1 INTRODUCTION	1
1.1 Motivation and Description	1
1.2 Outline of Thesis	2
Chapter 2 LITERATURE REVIEW	3
Chapter 3 METHODS	5
3.1 ISIS-CFD solver	5
3.1.1 Physical Modeling.....	5
3.1.2 Numerical Framework	7
3.2 Meshing Methodology	10
3.2.1 Meshing in Hexpress	10
3.2.2 Mesh Management	11
3.2.3 Mesh Manipulation to reflect motion of body	11
3.2.4 Rotating Frame Method	11
3.2.5 Sliding Grid	12
3.2.6 Overset Grid	12
3.2.7 Adaptive Grid Refinement.....	15
3.2.8 HPC Resources	15
3.3 KCS Geometry and Definition	16
3.4 Mesh Generation	16
3.4.1 Hull domain/s	17

3.4.2	Rudder Domain Mesh	19
3.4.3	Propeller Domain Mesh	21
3.4.4	Mesh Quality Check and Summary	22
3.5	Simulations	23
3.5.1	Boundary Condition	23
3.5.2	Body parameters	23
3.5.3	Adaptive Grid Refinement	24
3.5.4	Velocity Ramping	25
3.5.5	General Work Flow	26
3.5.6	Self Propulsion	26
3.5.7	Turning Circle	30
Chapter 4	RESULTS AND DISCUSSION	32
4.1	Self Propulsion	32
4.1.1	Validation	33
4.1.2	Free Surface elevation	35
4.1.3	Wake Flow	36
4.1.4	Vortical Structure Interaction	41
4.2	Turning Circle	43
4.2.1	Validation with EFD results	43
4.2.2	Free surface and Wake Flow	49
4.2.3	Vortical Structures	53
4.3	Mesh Analysis	55
Chapter 5	CONCLUSION	58
5.1	Future outlook	59
	Bibliography	61

List of Figures

3.1	Sliding Grid: Identification of Neighbour Cell	13
3.2	KCS Hull and with Rudder and Propeller	16
3.3	Coordinate System (Ship coordinate system in Red and fixed coordinate system in Black	17
3.4	Computational Grid Setups	18
3.5	Refinement Zones (in blue)	19
3.6	Section of YZ plane at X=0 of Hull Domain/s Mesh	19
3.7	Section of XZ plane at Y=0 of aft of the Hull Domain/s Mesh	20
3.8	Section of XZ plane at Y=0 of fwd of the Hull Domain/s Mesh.	20
3.9	Rudder and Propeller domain	20
3.10	Rudder Grid	21
3.11	Propeller Mesh.	22
3.12	AGR extents (X and Y in Blue, Z in pink)	25
3.13	Half Sinusoidal Velocity Ramp	25
3.14	Simulation Workflow	26
3.15	Converged of RPS using RFM.	27
3.16	Convergence of Propeller RPS using RPM.	28
4.1	Converged of X forces using RFM	32
4.2	Force Difference at Stern	33
4.3	Force and Pressure Difference at Stern	34
4.4	Free Surface elevation in Self Propulsion	35
4.5	Sections used to wake analysis	36
4.6	Self Propulsion using RPM - Vertical Cut-planes	37
4.7	Self Propulsion using RPM- Horizontal cut-planes.	39
4.8	Self Propulsion using RPM - Vertical cut-planes	40
4.9	Self Propulsion using RFM- Horizontal cut-planes.	41
4.10	Helicity plot of Self Propulsion ($Q^*=1000$)	42

4.11 Non-dimensional absolute vorticity - Z section at Rudder Propeller	43
4.12 Turning Circle Simulation	44
4.13 Forces and moments in the XY plane during Turning Circle	45
4.16 Free surface prediction.	49
4.17 Turning Circle using RPM - Vertical cut-planes	50
4.18 Turning Circle using RPM- Horizontal cut-planes	51
4.19 Turning Circle using RFM - Vertical cut-planes	52
4.20 Turning Circle using RFM- Horizontal cut-planes	53
4.21 Turning Circle vortical structure predictions ($Q^*=1000$)	54
4.22 Non-dimensional Absolute Vorticity - Z plane Rudder Propeller Section in turning circle (CG1).	55
4.23 Free surface refinement - Z plane Rudder Propeller Section of CG1 in turning circle- Mesh (left) and Non-Dimensional Absolute Vortex(right)	55
4.24 Free surface refinement - X plane Ship Propeller section of CG1 in turning circle- Mesh (left) and a zoom of mass fraction with mesh(right)	56
4.25 Intergrid refinement - X plane Ship Propeller section of CG2 in Self Propulsion- Mesh (left) and a zoom of mass fraction with mesh(right)	57
4.26 Mesh misalignment in CG1 (Self Propulsion) at the free surface intergrid boundary	57

DECLARATION OF AUTHORSHIP

I declare that this thesis and the work presented in it are my own and have been generated by me as the result of my own original research.

Where I have consulted the published work of others, this is always clearly attributed.

Where I have quoted from the work of others, the source is always given. With the exception of such quotations, this thesis is entirely my own work.

I have acknowledged all main sources of help.

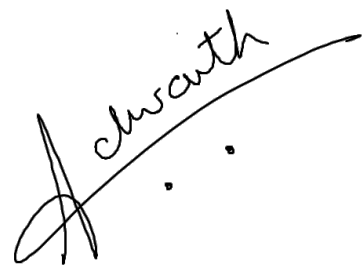
Where the thesis is based on work done by myself jointly with others, I have made clear exactly what was done by others and what I have contributed myself.

This thesis contains no material that has been submitted previously, in whole or in part, for the award of any other academic degree or diploma.

I cede copyright of the thesis in favour of Ecole Centrale de Nantes.

Date: 24 August 2020

Signature:

A handwritten signature in black ink, appearing to read "A. Schwath". The signature is written in a cursive style with a long, sweeping underline that curves to the right. There are two small dots below the signature.

INTRODUCTION

1.1 Motivation and Description

Commercial ship design until recently has focused on Resistance and propulsive power optimization as the main criteria for design. With higher demands for safety and the enactment of the IMO RESOLUTION MSC.137(76), the need for assessing the sea-keeping behaviour of the vessel has gained much importance.

Due to the highly viscous flow associated with the maneuvering simulations, the URANS and DES approaches have been preferred over inviscid solvers. Computational Fluid Dynamics (CFD) has proven to be a high fidelity and effective approach to predict ship motions in such complex maneuvers. As the method uses physical principles, the predictions are more accurate and demands almost no empirical data. With the advancements in parallelization, CPU memory and numerical algorithms, CFD has become the most used method for large domain simulations involving viscous flow.

Direct simulation which involves the rotating propeller, moving rudders and resolving all 6 dofs are the most reliable approach albeit the most complex for maneuvering simulation. Due to the small time-step requirement for resolution of propeller flow, such simulations demand high computational cost. Subsequently, limited studies are conducted on such maneuvering simulations. To reduce the computational cost, several approaches have been attempted by increasing the time-step requirement.

This work follows the SIMMAN 2020 workshop blind test case specifications for the KRISO Container Ship (KCS) in deep water for assessment of motions and forces in self propulsion and the 35 deg turning circle maneuver. The main focus of this work is the study of the Rotating Frame Method(RFM) which creates a pseudo-rotation of the propeller by modifying the momentum equation allowing the use of an higher time-step and to assess the accuracy of

predictions using direct simulation. The results are compared with the predictions using Actuator Disc and validated against Experimental data from MARIN. In addition, the work includes a study on the effect of using ship as overset with comparisons with ship meshed in background. The work has used multi-phase URANS ISIS-CFD flow Solver developed by METHRIC team of LHEEA laboratory which forms a part of FineMarineTM developed by Numeca.

1.2 Outline of Thesis

This thesis is structured in six chapters including the current. Chapter 2 describes the current literature. Chapter 3 initially describes the working of the ISIS-CFD solver and moves on to enumerate the work flow and setup parameters of the KCS Maneuvering simulation. It includes a description of the KCS hull and the trials and setbacks encountered through the project. Chapter 4 discusses the results of the Self Propulsion and the turning circle test. Finally Chapter 5 provides an overview of the results and observations/interpretations and finally suggestions for future work and development.

CHAPTER 2

LITERATURE REVIEW

The Manoeuvring of ships in deep water creates highly complex flows owing to the lateral motion of the ship and interactions between the hull, propeller and rudder. This generates highly viscous flow with vortical structure interactions and significant motions in all six dofs. CFD is a powerful tool in this regard as it provides an improved understanding of the physics of ship manoeuvring by providing information on both the flow field and the resulting forces on the hull and the appendages (ITTC 28 committee).

Direct simulations which involves modelling of the propeller have stringent requirements on time-step to resolve the propeller flow but require no empirical inputs. Due to complexity and cost, there have been a limited number of direct CFD simulations for ship maneuvers. To reduce the computational cost several studies have been dedicated to developing and validating mathematical models for manoeuvring predictions and uses CFD as a tool for computing hydrodynamic derivative. Sung et al (2015) performed virtual captive model tests with KCS and KVLCC to estimate linear and non-linear coefficients using STAR-CCM+. Though virtual captive time series showed good agreement with the experimental captive model test results, when compared to the free sailing results from the SIMMAN 2008 Workshop both the experimental and virtual method showed similar offsets in simulated turning circle and zigzag manoeuvres.

Approaches have been made to create a reduced model by increasing the time-step for resolving propeller flow to reduce the computational effort. A promising approach is the use of Rotating Frame Method (RFM). The first use of the RFM or the static rotor method in CFD was in the aerodynamic industry. The use of the RFM for prediction of the propeller thrust and flow in ships has been validated in many studies (Ngoc et al. 2019, Prakash and Subramanian 2010). The use of RFM for prediction of behaviour of vessel during sea-keeping manoeuvres are limited in literature. Queutey et al. 2017 used the RFM to simulate the ONR Tumblehome in head waves using ISIS-CFD flow solver. The results are in good agreement with the experimental and

direct simulation results. This shows the possible use of such reduced models for manoeuvring prediction but requires further validation for IMO manoeuvres.

With increasing computational power, studies using direct simulation have become more feasible though not to the point of industrial application owing to the exorbitant CPU time required for such simulations. These studies help understand the complex phenomena during IMO Manoeuvres such as vortical structure interactions between the propeller, rudder and the bilge. A good discussion of this phenomenon is presented in the study by Wang et al. 2016, who performed direct RANS simulation of the ONR Tubelhome for self Propulsion and Turning Circle using OpenFoam Naoe-FOAM-SJTU. Controllers were used for both propeller and rudder during Self Propulsion and turning circle simulations and the results were in good agreement with experimental data from IIHR. Shen et al. 2015 studied the 15/1 and 10/10 zig-zag manoeuvres of the HSVA KCS hull with rotating propeller using OpenFoam based solver with dynamic overset grid capability. The results show good agreement with the Experimental data.

The blind test case of the SIMMAN 2020 Workshop to simulate the self-propulsion and the turning circle maneuver of the KCS hull and rotating propeller in deep water using ISIS-CFD flow solver is studied in this work. A Proportional-Integral (PI) controller is used for predicting the required propeller RPS for maintaining velocity corresponding to $F_n=0.26$. The study uses a reduced model with RFM and direct simulation and compares the results with the Experimental data from MARIN. In addition, comments are made on the overset interpolation while using ship as overset by comparing with results with ship weighted transformation.

METHODS

3.1 ISIS-CFD solver

In this work, the ISIS-CFD solver is used to for solving the flow around bodies. The ISIS-CFD solver developed by the MEETHRIC((Modelisation Ecoulement Turbulent Haut Reynolds Incompressible et Couplage) research group is a finite volume (FVM) 2 fluid flow solver that solves the URANS incompressible equations. The entire numerical fluid model is considered to be comprised of 2 pure fluids, water and air, which are separated by an interface which here on will be referred to as the free-surface. The methodology used by the solver is based on the paper by Queutey and Visonneau 2007 and is described in the following sections.

3.1.1 Physical Modeling

3.1.1.1 Governing Equation

ISIS-CFD is capable of solving multi-phase flows and moving grids. Assuming incompressible flow under iso-thermal conditions, the governing equations to be solved are the mass conservation, momentum conservation and volume fraction conservation. These equations are shown below:

$$\frac{\partial}{\partial t} \int_V \rho dV + \int_S \rho(\vec{U} - \vec{U}_d) \cdot \vec{n} dS = 0 \quad (3.1a)$$

$$\frac{\partial}{\partial t} \int_V \rho U_i dV + \int_S \rho U_i (\vec{U} - \vec{U}_d) \cdot \vec{n} dS = \int_S (\tau_{ij} I_j - p I_i) \cdot \vec{n} + \int_V \rho g_i dV \quad (3.1b)$$

$$\frac{\partial}{\partial t} \int_V c_i dV + \int_S c_i (\vec{U} - \vec{U}_d) \cdot \vec{n} dS = 0 \quad (3.1c)$$

where V is the control volume, bounded by the closed surface with the unit outward normal vector \vec{n} moving with at velocity \vec{U}_d . \vec{U} and p represent the velocity and pressure fields respectively. τ_{ij} and g_i are the components of the viscous stress tensor and the gravity vector and I_j is a unit vector. c_i represents the volume fraction of the i^{th} volume fraction of the fluid i with $c_i = 1$

denoting the presence of the fluid and $c_i = 0$ denoting the absence.

The physical flow properties of the fluid (μ and ρ) are defined setting the following constitutive settings:

$$\rho = \sum_i c_i \rho_i \quad \mu = \sum_i c_i \mu_i \quad \sum_i c_i = 1 \quad (3.2)$$

Also, while considering a moving grid, the space conservation law is to be satisfied:

$$\frac{\partial}{\partial t} \int_V dV - \int_S \vec{U}_d \cdot \vec{n} dS = 0 \quad (3.3)$$

Assuming that the density of the fluids remains constant, the mass conservation equation is simplified using the generalized Gauss' theorem as:

$$\nabla \cdot \vec{U} = 0 \quad (3.4)$$

3.1.1.2 Turbulence Closure

The Navier Stokes equation can only be resolved completely on fine computational grids with small time steps when the Reynold's number is low. In order to overcome this problem, a fluctuating quantity ϕ is decomposed using time averaging operator as :

$$\phi = \bar{\phi} + \phi' \quad (3.5)$$

where $\bar{\phi}$ is the steady value or the average value and ϕ' is the fluctuation.

This decomposition leads to an additional 6 unknowns in the form of time averages of fluctuation in velocities ($\overline{u_i u_j}$) resulting in a total of 10 unknowns and 4 equations. Following this approach, we obtain the new a new term called the reynolds tensor $\tau_{t_{ij}}$ containing terms of time-average of product of velocity fluctuations (the 6 new unknowns).

$$\tau_{ij} = \tau_{l_{ij}} + \tau_{t_{ij}} \quad (3.6)$$

$$\tau_{l_{ij}} = 2\mu S_{ij} \quad \tau_{t_{ij}} = \overline{\rho u'_i u'_j} \quad (3.7)$$

where S is the mean strain-rate tensor. Closure of turbulence equations is done by modeling a relation between the time-averaged product of velocities with time averaged velocities and pressure. Isotropic turbulence closures are based on the Boussinesq hypothesis related to eddy viscosity which states the Reynolds stress tensor is linearly proportional to the mean strain-rate.

Subsequently, the turbulent terms of the mean strain-rate is define as:

$$\tau'_{ij} = 2\mu_t S_{ij} - 2/3\rho K \delta_{ij} \quad (3.8)$$

where μ_t and K are the turbulent viscosity and kinetic energy respectively. This formulation leads to a reduction from 6 new unknowns to 2.

The value of K and μ_t are obtained using turbulent eddy viscosity models by solving transport equation. There are various models that can be found in literature defined over the length(L) and velocity(V) scale and a brief is given below:

- 0 transport equation: the velocity and length are known and μ_t is approximated as ρLV
- 1 transport equation: Length is know and the velocity is resolved form 1 transport equation: $\mu_t = \rho L \sqrt{K}$
- 2 transport equation: Velocity and Length are resolved using 2 transport equations and $\mu_t = \rho c \frac{k^2}{\epsilon}$ where ϵ is the turbulent dissipation.

The **K- ω SST Menter** is a 2- transport equation turbulence model proposed by Salvesen 1978. The basic principle of the K- ω SST Menter closure is to use k- ϵ model propsed by Jones and Launder 1972 in the far-field and keep the k- ω Wilcox model proposed by Wilcox 1988 elsewhere in the domain thus improving the predictions of the boundary conditions on the outer limits.

3.1.2 Numerical Framework

3.1.2.1 Discretization form

To solve the Navier Stokes equation, ISIS-CFD uses the Finite Volume Method. The global domain is subdivided into a finite number of non-overlapping control volumes called cells, whose centroids are the location of the computed variables from the Navier-Stokes discretization. With the variables of interest located inside the volume, the control volume can have arbitrary shapes with any number of faces. Moreover, the number of cells can be arbitrary and the NS equations should be satisfied in each of these cells. The Finite element Method is a conservative method as the flux entering a cell should be equal to the flux leaving the adjacent cell.

For second order accuracy, the volume and surface integrals are approximated by substituting the quantity Q with its 1st order Taylor expansions giving the approximation as:

$$\int_V Q dV = \int_V (Q_p + (x - x_p) \nabla Q_p) dV \approx \int_V Q_p dV \quad (3.9a)$$

$$\int_S Q \vec{n} dS = \sum_f \int_S Q_f \vec{n} dS \approx \sum_f Q_f \vec{n} dS \quad (3.9b)$$

Subsequently, the second-order accurate semi-discretized transport equation for cell center C and faces f can be written as:

$$\underbrace{\frac{\partial}{\partial \tau} (\rho V Q)_C}_{\text{fictitious time step}} + \underbrace{\frac{\partial}{\partial t} (\rho V Q)_C}_{\text{Real time step}} + \sum_f (\underbrace{CF_f}_{\text{Convective fluxes}} - \underbrace{DF_f}_{\text{Diffusive fluxes}}) = \underbrace{S_Q^V}_{\text{Volume source}} + \sum_f \underbrace{S_Q^f}_{\text{Surface source}} \quad (3.10)$$

The pressure term acting on the surface are included in the surface source term

The convective and diffusive fluxes are define as:

$$CF_f = \dot{m}_f \quad \dot{m}_f = \rho (\vec{U} - \vec{U}_d) \cdot \vec{S}_f \quad DF_f = (\Gamma_Q)_f (\nabla Q_f I_j) (S_j)_f \quad (3.11)$$

where Γ_Q is the isotropic or anisotropic diffusion coefficient and I_j is a unit vector.

The fictitious time derivative is used to improve the convergence within the non-linear loop evaluated as:

$$\frac{\partial Q}{\partial \tau} = \frac{Q^c - Q^{c0}}{\Delta \tau} \quad (3.12)$$

where Q^{c0} is the previous estimation of Q^c in the non-linear iteration.

The time derivatives are evaluated using a 3 level Euler 2nd order accurate approximation:

$$\frac{\partial Q}{\partial t} \approx \frac{\delta Q}{\delta t} = e^c Q^c + e^p Q^p + e^q Q^q \quad (3.13)$$

where c refers to the current time t^c , p the previous time t^p , and q the time t^q anterior to p .

Combining the temporal discretization with the semi-discretized equation, we get the fully discretized form of the transport equation:

$$(e^c + \frac{1}{\Delta \tau}) (\rho V Q)_C^c + \sum_f (CF_f - DF_f) = S_Q^V + \sum_f (S_Q^f) - (e^p \rho V Q)_C^p - (e^q \rho V Q)_C^q + \frac{(\rho V Q)_C^{c0}}{\Delta \tau} \quad (3.14)$$

3.1.2.2 Scheme for Reconstruction of values at Face

ISIS-CFD has implemented several schemes of which the reconstruction scheme used in this work is the AVLSMART scheme. The AVLSMART scheme is used for the discretisation of the convective fluxes in the momentum equation and the equation for turbulence modelling.

The AVLSMART scheme is a modified SMART scheme proposed in Przulj and Basara n.d. based on the 3rd order Quadratic Upwind Interpolation for Convective Kinematics (QUICK) algorithm proposed by Leonard 1979. It is a bounded convection scheme for unstructured grids based on the normalized variable formulation, which ensures monotonicity criteria needed to guarantee the boundedness criterion. The AVLSMART scheme has demonstrated to have an improved convergence behaviour without loss of accuracy in many situations.

3.1.2.3 Velocity Pressure Coupling

In the NS equations, the velocity of the domain is computed by solving the mass conservation equation and pressure is obtained by solving the momentum conservation equation. In order to have a coupling of pressure and velocity, the mass conservation equation is include the momentum conservation.

ISIS-CFD used weakly coupled algorithm based on the SIMPLE algorithm proposed by Rhie and Chow 1983 to couple the pressure and velocity that is the convergence to the actual pressure and velocity is achieved through non-linear iterations. The method takes into account pressure gradient discontinuity by using pressure equation based on $\frac{\nabla p}{\rho}$ rather than ∇p ensuring more stability to the solution in the presence of a density discontinuity.

The semi continuous form of the momentum equation can be written from 3.14 as:

$$\left(\begin{array}{l} (e^c + \frac{1}{\Delta\tau}) (\rho V \vec{U})_C^c + (e\rho V \vec{U})_C^p + (e\rho V \vec{U}')_C^q + \\ a_C \vec{U}_C^c + \sum_{nb} a_{nb} \vec{U}_{nb}^c + \vec{S}_C + (V \vec{\nabla} p)_C^c \end{array} \right) = (\rho V)_C^c \vec{g} + \frac{(\rho V)_C^c (\vec{U})_C^{c0}}{\Delta\tau} \quad (3.15)$$

where a_C and a_{nb} are the matrix coefficients form the implicit part of the diffusive and convective terms, \vec{S} is the source term containing all explicit remaining contributions and external force files except gravity and pressure.

Consequently, an equation for the velocity field at the center of the control volume can be obtained from the discretized momentum equation 3.14 as :

$$\vec{U}_C^e = -Cp_c \left(\vec{U}_C + \left(\frac{\vec{\nabla} p}{\rho} \right)_C - \vec{g} \right) + \frac{Cp_c \vec{U}_C^{c0}}{\Delta\tau} - \frac{Cp_c \left((eV\rho\vec{U})_C^p + (eV\rho\vec{U})_C^q \right)}{(\rho V)_C^c} \quad (3.16)$$

$$\text{where } Cp_c = \left(e^c + \frac{1}{\Delta\tau} + \frac{a_c}{(\rho V)_C^c} \right) \quad \text{and} \quad \vec{U}_C = \frac{\sum_{nb} a_{nb} \vec{U}_{nb} + \vec{S}_C}{(\rho V)_C^c} \quad (3.17)$$

The velocity at the faces can be obtained with the similar expression. The pressure field is obtained by substituting 3.16 in the mass conservation equation. This ensures that the volumetric flux defined by the interpolation will be conservative provided the pressure equation is satisfied.

3.2 Meshing Methodology

3.2.1 Meshing in Hexpress

The initial computational grid is generated using HEXPRESSTM, which is the automatic unstructured hexahedral mesh generator tool incorporated in FINETM/Marine. This tool is capable of generating complex 2D and 3D unstructured meshes. The mesh for each domain is generated separately following the steps described below:

- **Initial Mesh:** This step defines the base cell size of the domain. All the following steps depend on the size defined in this step. Creating cells of small sizes in this step can lead to high computation time. So, finding the optimum size for the given problem is important.
- **Adapt to Geometry:** This is a more localized step where the geometry of interest is meshed. The cells inside the geometry of interest are removed. Additional refinement of mesh is done in the zones of interest. The refinement (defined as number of steps) is done by cell division and so is dependent on the base cell size defined in the initial mesh. The diffusion of the refinement is also important for a gradually increase in size of the cell moving away from the area of interest.
- **Snap to Geometry:** In this step the the boundary cells close to the geometry of interest are snapped on to the boundary surface.

- **Optimize:** After the snapping step, some of the resulting cells will have undesired cell geometry such as orthogonality and skew . This step optimises and where necessary, removes such geometry.
- **Viscous Layer:** This divides the cells close to boundary of the geometry of interest into layers to capture the viscous effects produced in the flow.

3.2.2 Mesh Management

This section deals with the methodology used to modify the computational grid by ISIS-CFD during the simulation.

3.2.3 Mesh Manipulation to reflect motion of body

When a body moves either by imposed motion or as a result of the solved degree of freedom, the surrounding meshes are to be modified. This modification can be reflected as described in the two ways:

3.2.3.1 Rigid Motion

In this setting, the domain mesh, follows the motion of the body body without being deformed. This method enables any arbitrary displacements but the number of bodies is constrained to one per domain. This method modifies the limits of the domain and so it is used in combination with a background grid which is fixed.

3.2.3.2 Weighted Deformation

The mesh is distorted using a weighted-distance method in order to displace the body into its new position. The distortion is done in such a way that the deformation at the body is the 1, i.e. the greatest, while the deformation at the boundaries are 0, i.e. no distortion. This method does not modify the limits of the domain as the mesh is distorted and not transformed/rotated.

3.2.4 Rotating Frame Method

The rotating frame method is used to model the rigid body rotation of a body by solving the RANS equation in a rotating frame but with quantities expressed in the inertial reference. This is

done by modifying the Momentum equation as follows:

$$\frac{\partial}{\partial t} \int_V \rho U_i dV + \int_S \rho U_i (\vec{U} - \vec{U}_d) \cdot \vec{n} dS = \int_S (\tau_{ij} I_j - p I_i) \cdot \vec{n} dS - \int_V \rho (\Omega \times \vec{U})_i dV + \int_V \rho g_i dV \quad (3.18)$$

where Ω is the rotation velocity.

Notice that $\int_S \vec{U}_d \vec{n} dS = 0$ as domain is undergoing rigid body motion. The boundary conditions may be defined both in body and earth-fixed reference system.

Unsteady flows can be modelled with reasonable accuracy using this approach for instance the unsteadiness coming from the flow pattern. As this method does not involve rotating the grid itself, it requires much less computational effort compared to the sliding grid method.

3.2.5 Sliding Grid

For a full viscous simulation of unsteady flow on system like the hull/propeller system, the sliding grid method is used which involves the actual rigid body rotation of a domain. This puts severe requirements on the grids and coupling techniques which will have to be general and accurate to deal with complex fully-unstructured grids around the hull and the full propulsive system.

The implementation of sliding grid method does not ensure flux conservation at the connection between the 2 domains. To compute the fluxes over the sliding interface, the connections between cells on the 2 sides of the interface is to be established. This is done at each time step in order to account for the rotation of the 2 subdomains with respect to each other. For each cell and face on the interface, a search for the best matching cell center is conducted over on the other subdomain. This cell is then used as a neighbor cell for the flux computation. The steps involved are as shown in figure 3.1 It is necessary to have a small time step so that that a cell from one domain does not travel faster than one cell per time step from the other domain to ensure the exchange of information between 2 non-matching domains is performed correctly.

3.2.6 Overset Grid

The Overset grid approach utilizes a set of grids that encompass the computation domain and overlap each other without requiring point-matched connectivity between individual grids. CFD solution on the system of grids requires coupling the solution between grids in the overlapped

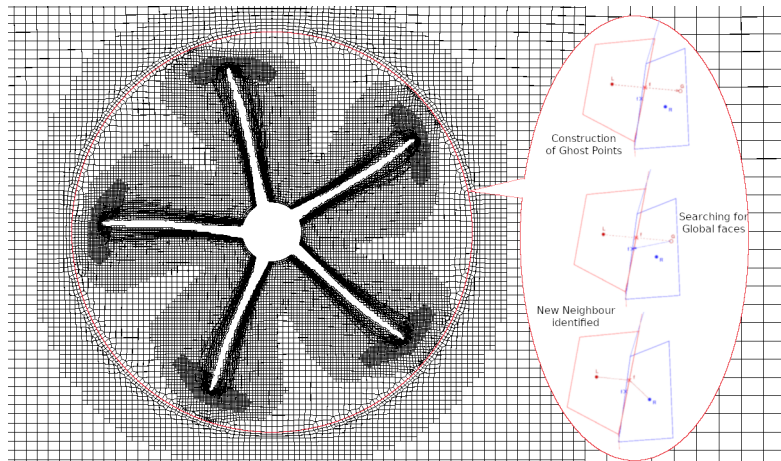


FIGURE 3.1. Sliding Grid: Identification of Neighbour Cell

regions. This is performed by identifying appropriate intergrid boundary locations in one grid and obtaining the value to be applied by interpolating the solution from grids that overlap the region. The domain connectivity information consists of the locations that are to be excluded from the computation, the location of the intergrid boundary locations, and the corresponding interpolation sources. This domain connectivity information is computed by a process call as overset grid assembly.

3.2.6.1 Overset Boundary Identification

The preliminary requirement for implementation of the overset requires the identification of the overset domain and body boundaries. The implementation in ISIS-CFD assumes that each overset domain consists of only one body and multiple body definitions in the overset domain is not supported. The implementation uses an implicit method of identification of the domain boundaries. The domain boundary is formed from all the patches not belonging to the body as well as all the patches belonging to the body explicitly declared by the user as being part of the domain boundary. All patches belonging to a body except those belonging to a virtual body or a sliding patch form the domain body.

3.2.6.2 Cell Status

Each cell during overset computation is given one among 3 status:

- Active: The governing equation is normally solved for this cell
- Blanked: This is cell is ignored in computation

- **Interpolated:** The value of this cell is updated from active cells located in another overlapping domain.

The implementation for assigning cell status is done using a simple procedure locally at each bloc without any MPI communication. For this, each domain is declared as either a background domain or an overlapping domain. Through this implementation, there are 3 possible types of overlaps which are detailed below:

- **Background domain -Overlapping domain overlap:**

All the cell status in the overlapping domain are assigned active status. The boundary cells are assigned with interpolation status. In the background domain, all the cells inside the overlapping domain are given a blanked status and all the active cells are propagated one layer into the hole region. Then the status of the blanked cells next to active cells are changed to interpolated cells.

- **Overlapping domain -Overlapping domain overlap:**

The implementation assumes that each domain one body defined and that the overlapping domains do not have overlapping bodies. In a given overlapping domain a cell is assigned active if the distance of the cell from the body in the domain is closer than the body in the other overlapping domain otherwise the cell is assigned a blanked status. After propagating the active cell by one layer into the blanked region, the blanked cell next to the active cell is assigned an interpolated status.

- **Background domain -Background domain overlap:**

This case has not been implemented as the domain to be given importance is unknown.

3.2.6.3 Overset Interpolation

The critical issues of overset implementation lies in assignment of the interpolated values. Though higher order interpolation is preferred, the problem lies in the stability of such schemes. To ensure a robust implementation of overset interpolation, a compromise between accuracy and stability is done. Two interpolation schemes have been implemented in the solver.

- **Least Square Approach:** This scheme ensures a second order accuracy but suffers from numerical stability
- **Weighted Distance Approach:** This a first order interpolation scheme which ensure stability

Through the default scheme is the higher order scheme, a minimum interpolation coefficient is specified such that if it is smaller than the threshold value, the lower order scheme is employed.

3.2.7 Adaptive Grid Refinement

Adaptive grid refinement (AGR) is an iterative process that refines the grid dynamically as per the requirements of the solution as the simulation progresses. The adaptive grid refinement is a powerful tool having a wide range of applications. For the purpose of this work, we focus on the 2 major components of the adaptive grid refinement:

- **Capture Flow details:** As AGR is a local process, it is capable of capturing the free surface much more efficiently by inserting fine cells normal to free surface tensor. AGR reduces the size of the required mesh by reducing the initial refinement of the free surface and dynamically refining and where necessary, combining cells.
- **Refinement of Overset Boundaries:** AGR refines the cells at the intergrid boundary assuring a better overset interpolation between domains.

3.2.8 HPC Resources

The computations in this study are carried out on LIGER HPC cluster from LHEEA. Liger is the largest and most energy efficient computational resource available in western french region. The cluster has 252 nodes for dedicated for computation and 14 cores for visualisation with each node having 24 cores. It has a total Memory of 36 terabytes dedicated to computation. To submit a job for the computations , a script is used, in which the number of processors (multiple of 24) and the path to the executable file are specified . The maximum computation time allowed is 4 days per job though it is recommended to run a job for 1 day.

Choosing a convenient number of processors for a particular job is important. Experience using ISIS-CFD flow solver shows that selecting the number of processors such that 40000 to 80000 cells are assigned per partition is an optimal choice. Clearly, setting a very high number of processors does not mean necessarily considerable reduction in the computation time. In fact, the time needed for the communication between processors needs to be taken into account in that case.

Particulars	Unit	Model Scale	Particulars	Unit	Model Scale
Model			Rudder		
Lpp	m	6.0702	Type	Semi-balanced horn rudder	
Lwl	m	6.1355	S	m ²	0.0801
Bwl	m	0.8498	Lat Area	m ²	0.0379
D	m	0.5015	Turn rate	deg/s	14.28
T	m	0.285	Propeller		
Displacement	m ³	0.9565	Type	Fixed Pitch	
S w/o rudder	m ²	6.6381	No. blades	5	
CB		0.651	D	m	0.2085
CM		0.985	P/D	0.997	
LCB (fwd+)	(%)	-1.48	Rotation	Right hand	
Scale		1:37.89			

TABLE 3.1. Model Particulars

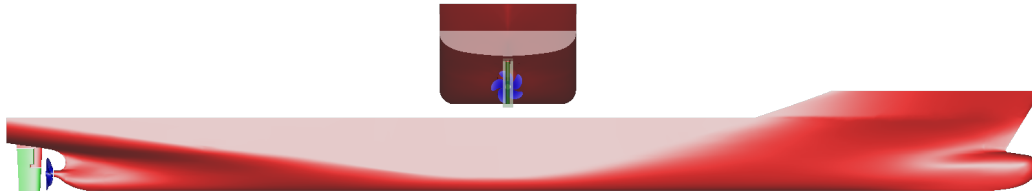


FIGURE 3.2. KCS Hull and with Rudder and Propeller

3.3 KCS Geometry and Definition

The case studied is a blind test case of the SIMMAN 2020 workshop. The KCS is a container ship designed by KRISO from Korea. The KCS is extensively used in the academic circle due to the complex geometry and availability of experimental results for validation. The model, propeller and rudder particulars are given in table:3.1

Right handed Cartesian coordinate system is employed to describe the motion of the ship. Each body has its own moving reference frame having the same orientation as shown in the figure along with a earth fixed reference frame.

3.4 Mesh Generation

The computational grid consist of three bodies. Accordingly the domains of the computational grid are:

- The Ruder domain
- The Propeller domain

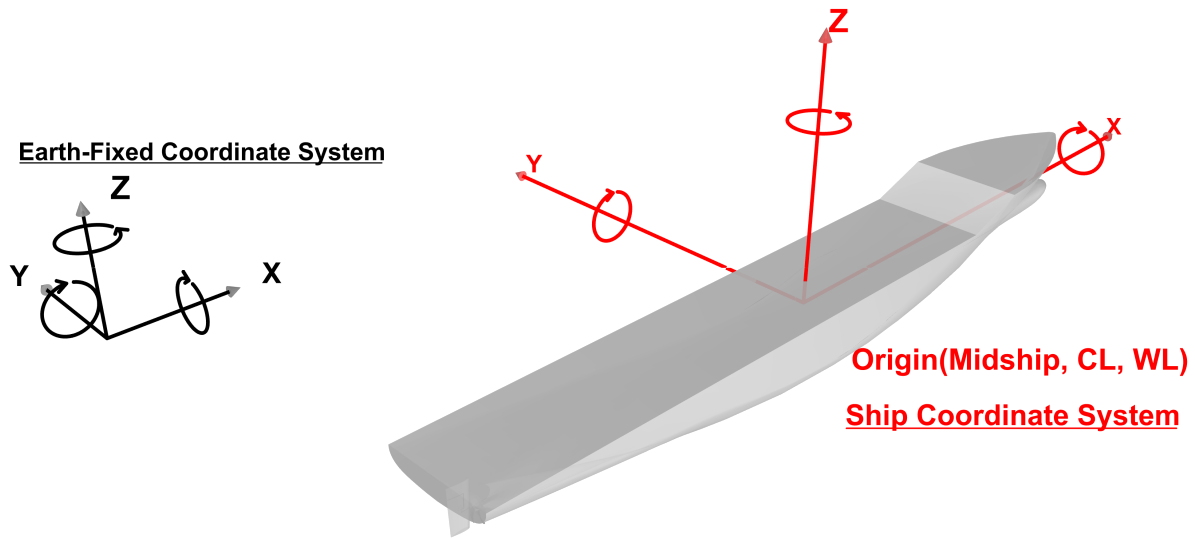


FIGURE 3.3. Coordinate System (Ship coordinate system in Red and fixed coordinate system in Black)

	$X \left(\frac{x}{L_{pp}} \right)$		$Y \left(\frac{y}{L_{pp}} \right)$		$Z \left(\frac{z}{L_{pp}} \right)$	
	min	max	min	max	min	max
CG1	-20.27	14.93	-12.50	12.50	-10.00	6.00
CG2	-19.20	19.20	-12.00	12.00	-7.80	3.40

TABLE 3.2. Physical Extents of Hull domain in meters

- The Hull domain*: This study is conducted using 2 different mesh setups, one with the ship as an overset domain in a background mesh domain(hereafter referred to as computational grid 1 or CG1), and, one with the ship and the background meshed in the same domain(hereafter referred to as computational grid 2 or CG2). The former enables the rigid motion of the mesh along with body motion thus maintaining the quality of the mesh cells but has the disadvantages related to overset interpolation. The latter uses weighted deformation to reflect body motion hence allowing limited motion of the body.

The coordinate system used is a right-handed coordinate system as shown in figure 3.3.

3.4.1 Hull domain/s

The physical domain extents of the two grids are shown in table 3.2. In CG1, the hull domain is comprised of the background domain which defines the extents of the computational domain and an overset hull domain as shown in the figure 3.4. The size of the ship domain is such that

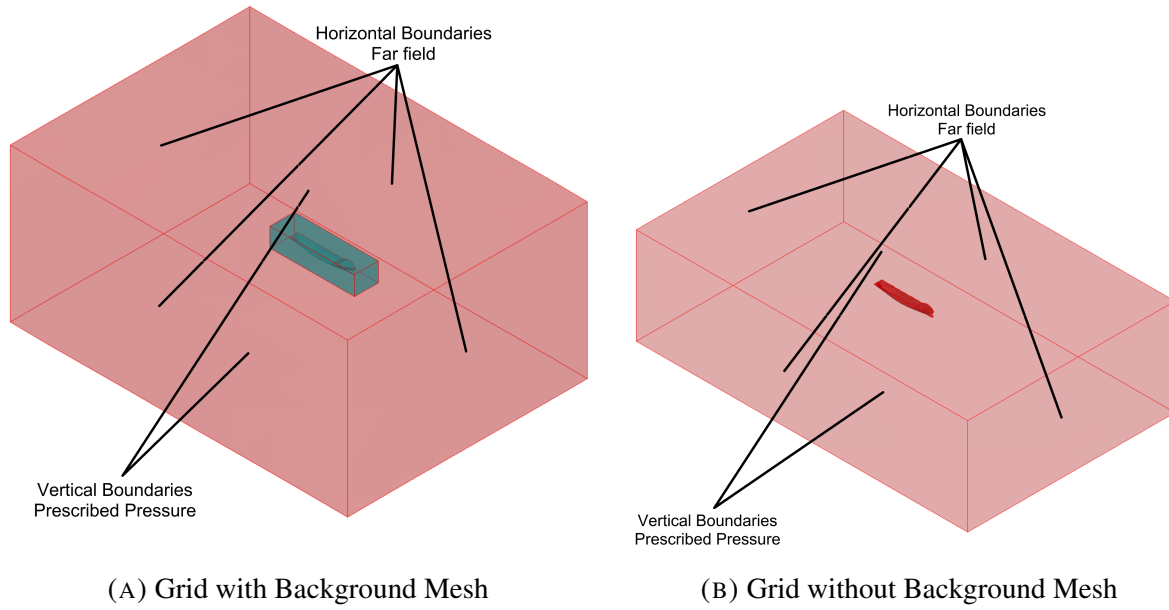


FIGURE 3.4. Computational Grid Setups

$\mathbf{X} \left(\frac{x}{L_{pp}} \right)$		$\mathbf{Y} \left(\frac{y}{L_{pp}} \right)$		$\mathbf{Z} \left(\frac{z}{L_{pp}} \right)$	
min	max	min	max	min	max
-4.40	4.40	-1.25	1.25	-1	1

TABLE 3.3. Ship domain extents in With background domain mesh in meters the cell sizes at the boundaries are uniform and devoid of refinement diffusion propagation. The dimensions of the ship domain are shown in table 3.3

For both computational grids the method and parameters of meshing of the surfaces is identical unless explicitly specified . The ship surfaces are comprised of the hull, deck, rudder stock, transom and the sliding grid interface. As we are not concerned with flow on the deck, we assign the deck with a slip boundary condition thus avoiding the need of viscous layer on this surface. With exception of the sliding grid interface and the deck, the other surfaces mentioned previously are assigned with wall function boundary condition. To capture viscous effects, the hull is meshed with a first viscous layer 0.0013 m thickness corresponding to 4 layers. To capture the free surface, the grid spacing required in z direction is taken as $\frac{\Delta z}{L_{pp}}$. The refinement in X and Y direction is limited by assigning an aspect ration of 200 to diffuse the computations effort. The global meshing details are shown in table 3.4

	Domain	X	Y	Z	Max Refinement	Diffusion
With background	hull	33	10	10	9	3
	background	33	25	20	8	2
Without background	hull + background	80	56	32	10	3

TABLE 3.4. Hull domain mesh details



FIGURE 3.5. Refinement Zones (in blue)

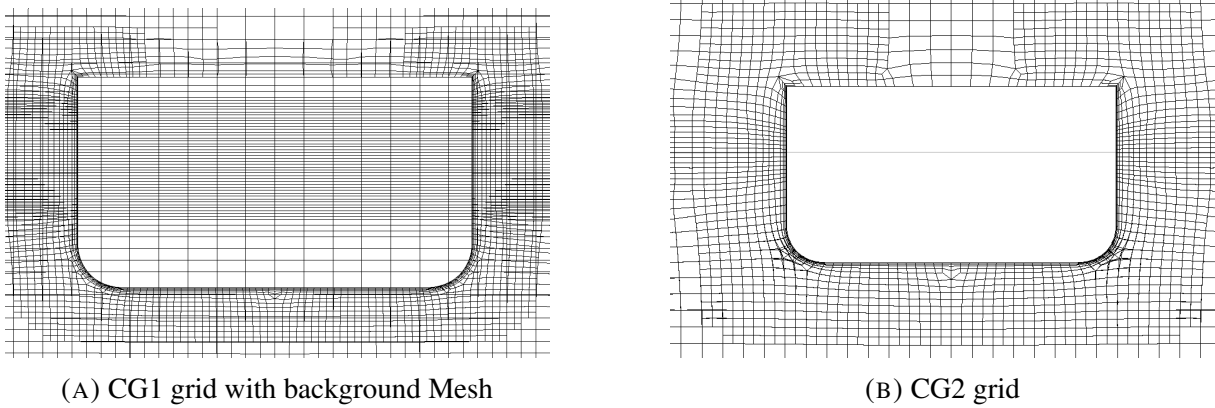


FIGURE 3.6. Section of YZ plane at X=0 of Hull Domain/s Mesh

In CG1, the initial mesh size values were computed such that the initial grid of the background and the ship are aligned for a acceptable interpolation between the two grids. The zonal refinements are used at locations shown in figure 3.5. These zone are:

- The bow of the ship owing to its complex geometry and to study the wave making phenomena of the bow.
- The aft of the ship due to the complex wake flow
- The rudder and propeller region to analyze the complex flow in hull and propeller wake and to have a better interpolation stencil for overset domains.
- For CG1, an additional free surface zonal refinement is performed. This ensures fine cells at the free surface when the ship domain rotates (trim/heel).

The resultant mesh can be observed in Figure 3.6, Figure 3.7 and Figure 3.8 s. The alignment of the background mesh with the hull mesh can be observed in figure 3.6a.

3.4.2 Rudder Domain Mesh

The rudder domain is a rectangular domain with dimensions $\frac{L_{pp}}{27.34} \times \frac{L_{pp}}{94.85} \times \frac{L_{pp}}{19.90}$ enclosing the rudder. To get a good resolution of flow over the rudder foil during the turning circle test a first

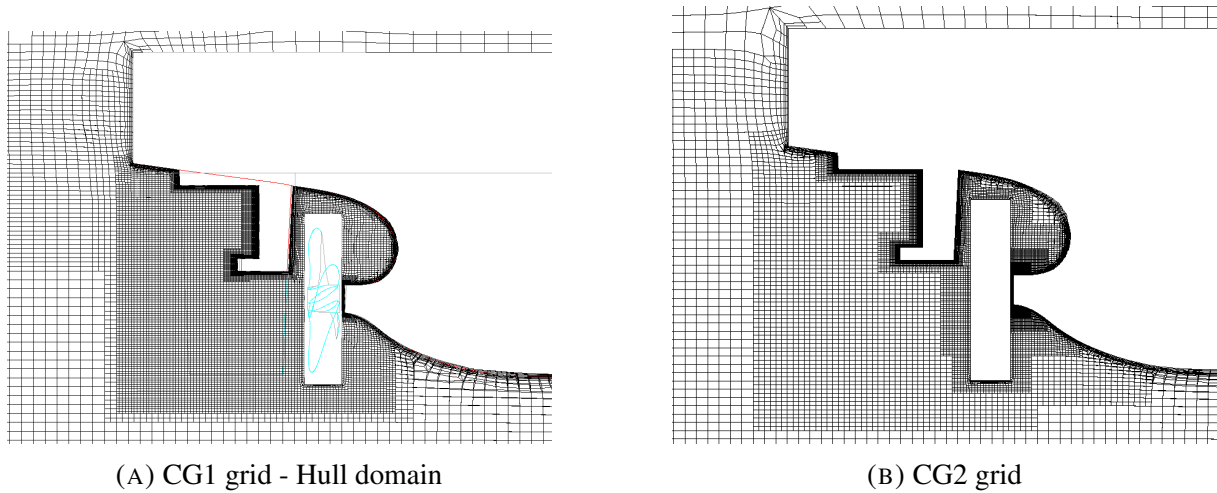


FIGURE 3.7. Section of XZ plane at $Y=0$ of aft of the Hull Domain/s Mesh

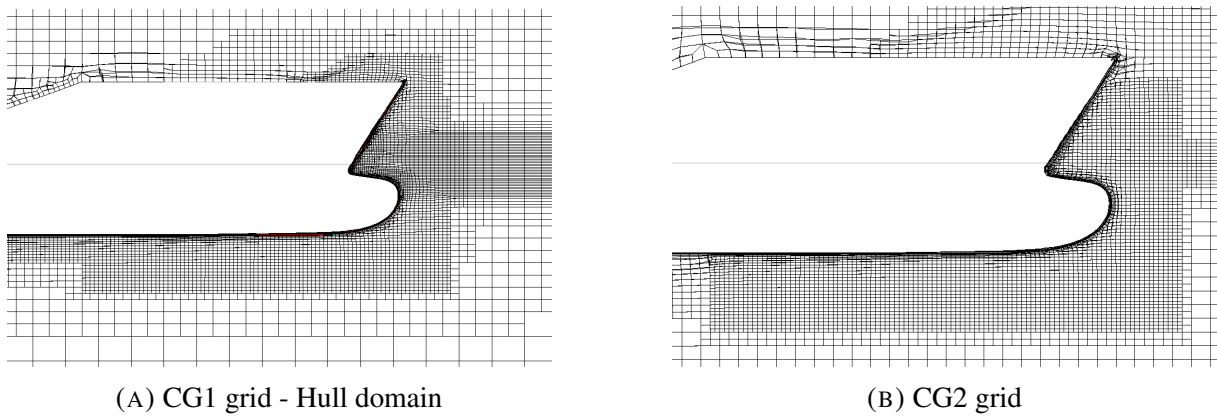


FIGURE 3.8. Section of XZ plane at $Y=0$ of fwd of the Hull Domain/s Mesh

viscous layer thickness of 0.000075 m corresponding to 10 layers is inserted. The inputs used for generating the mesh are detailed in table 3.6.

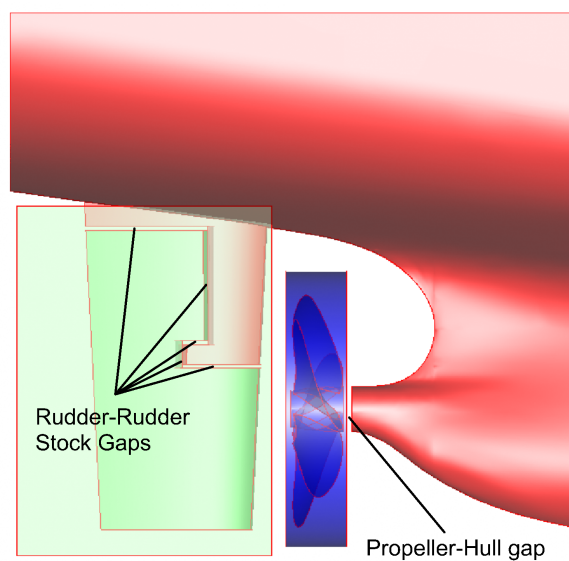


FIGURE 3.9. Rudder and Propeller domain

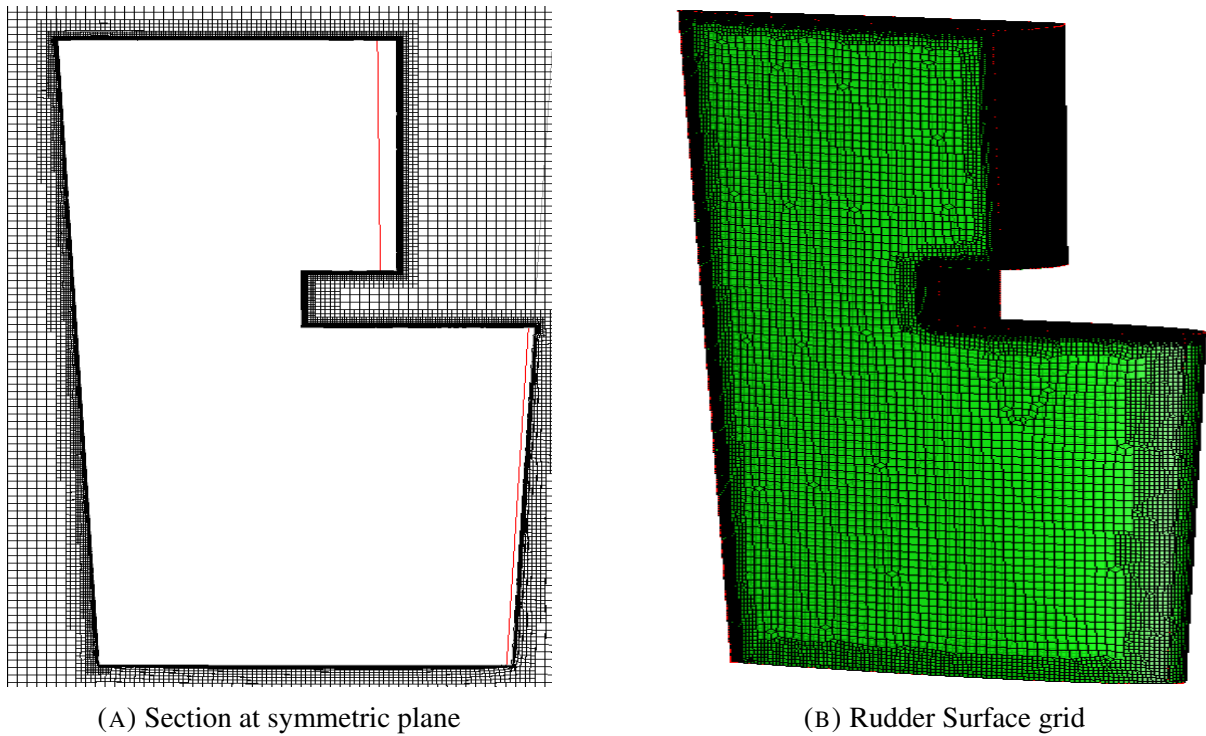


FIGURE 3.10. Rudder Grid

X	Y	Z	global refinement	refinement diffusion
71	20	98	3	2

TABLE 3.5. Rudder domain Mesh Details

Of particular interest in the rudder domain are the "gaps" between the rudder stock in the hull domain and the rudder in the rudder domain as can be seen in figure 3.9. These zones of interest are further refined to have a better overset interpolation. The resulting grid with refinement at the gaps can be observed in figure 3.10

3.4.3 Propeller Domain Mesh

The propeller domain mesh is a cylindrical mesh owing to the need of rotation of the domain. The length of the domain is $0.25D_p$ and diameter of the domain is $1.15D_p$ where D_p is the diameter of the propeller. In figure 3.9, a gap between the hull and the propeller can be observed. This is done so that the propeller and ship are 2 separate closed bodies. In this way, the actual forces acting on the hull and the propeller are obtained more accurately.

The propeller has a complex geometry owing to the skew of the blades and the sharp edges. The mesh should be fine to capture these details. In addition, the tips of the blades should be highly refined to capture the vortex shedding phenomenon. The details are shown in the table below:

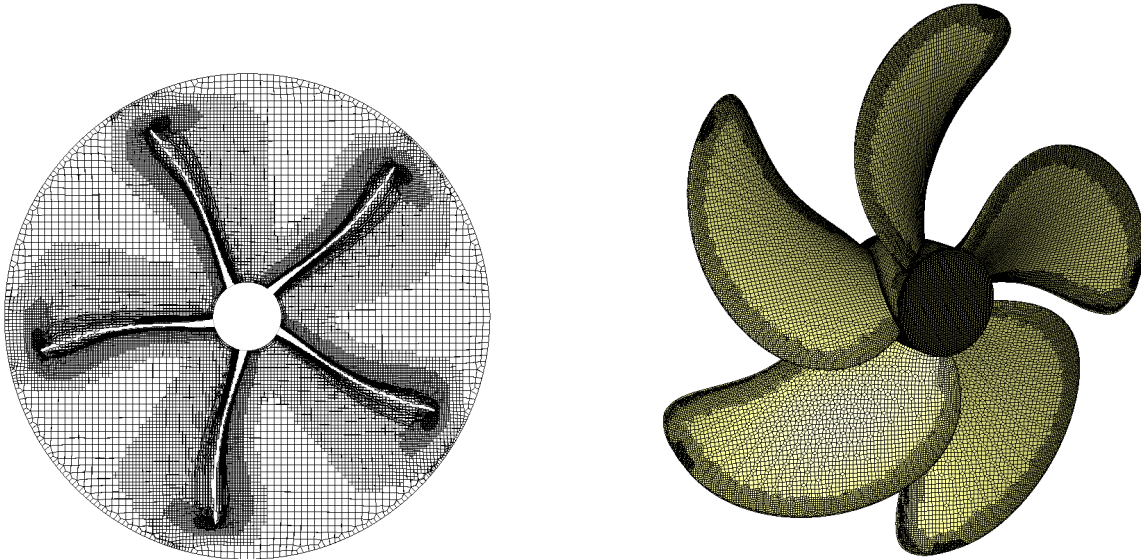


FIGURE 3.11. Propeller Mesh

X	Y	Z	global refinement	refinement diffusion
16	72	72	3	3

TABLE 3.6. Propeller domain Mesh Details

The generated grid can be observed to have snapped to the complex geometry of the propeller optimally capturing the sharp edge [figure 3.11]. The high refinement and the associated diffusion of the propeller tips can also be observed. It is desirable to have cells of same size at domain boundaries. In this case, the propeller tip refinement has not completely diffused at the boundaries. This problem can only be solved by increasing the size of propeller domain boundary. Due to the lack of space at the aft of the hull as can be observed from figure 3.9, this is not possible.

3.4.4 Mesh Quality Check and Summary

Before proceeding to simulation, the quality of the grids generated should be assessed. The quality of the grid is important as it directly affect the results and in some cases, leading to simulation crash or instabilities in the solution. A summary of the grid checks for all the domains are tabulated in table 3.7.

The minimum criteria for the computational grid is that there should be no Negative cells, Twisted cells or concave cells and the minimum angle of orthogonality should be higher than 5 deg. Table 3.7, show that both CG1 and CG2 satisfy this criteria. The cell counts of the resulting grids are given in table 3.8

Domain	CG1	CG2
Hull	4548304	4587131
BG	733841	
Prop	1260514	1260514
Rud	1122717	1122717
Total	7665376	6970362

TABLE 3.8. Grid Cell Summary

Domain/Criteria	Propeller		Rudder		Hull		
	CG1	CG2	CG1	CG2	CG1		CG2
					Hull	Background	
Negative Cells	0		0		0	0	0
Twisted Cell	0		0		0	0	0
Concave Cells	0		0		0	0	0
Orthogonality min angle (deg)	7.23		15.22		16.16	90	18.12

TABLE 3.7. Domain Grid Quality Check

3.5 Simulations

3.5.1 Boundary Condition

The boundary conditions assigned to the external surfaces are shown in figure 3.4. To avoid wave reflection at the boundaries, the horizontal boundaries are assigned with a far field condition with velocities in all 3 directions set to 0. This is also called the Dirichlet-Neuman condition. The vertical boundaries are assigned with prescribed pressure condition with updated hydrostatic pressure meaning thus allowing fluid to enter or exit the boundary.

The external boundaries of hull domain in CG1 and the rudder domain for both CG1 and CG2 are assigned as overset boundaries. As mentioned in the previous section, all the surfaces that define bodies are assigned with wall function except for the deck which is assigned with a slip condition.

3.5.2 Body parameters

The simulation consists of three bodies namely the hull, the rudder and the propeller. Here the main body is considered as the hull and the other 2 bodies have a connection(or joint) with the hull. Hence it is sufficient to define the parameters of the hull. The main parameters to be defined are the center of gravity(COG) and the diagonal components of mass matrix of the the hull along

with the connect bodies. The mass and the X and Y components of the hull is computed from the net displacement of the whole ship at at static equilibrium. the vertical position of the COG and the radius of gyration in all 3 axis is an input data for a given problem. These are obtained from the SIMMAN2020 Problem definition. The input parameter for hull body motion are tabulated in table 3.9

Mass (kg)	Center of Gravity (m)			Inertia (kg m^2)		
	X	Y	Z	I_x	I_y	I_z
958.736	-0.092	0.000	0.093	110.815	2351.180	2351.180

TABLE 3.9. Mass Matrix and Center of Gravity details

Pin joints are used for the connections to the main body so that the connected bodies are free to rotate. The bodies are connected to the hull at their respective centroids so that forces from the hull does not create moments in the bodies. Pin joints are used for the connections so that the connected bodies are free to rotate. The details of the connection points are given in table 3.10

	Pin Joint			Rotation Axis
	X	Y	Z	
Rudder	-3.0351	0	0	Z
Propeller	-2.929	0	-0.177	X

TABLE 3.10. Rudder and Propeller Connection

Another important connection to be specified is the sliding grid connection with the hull as the sliding grid domain does not foam a part of the hull. The solver uses a method where the sliding grid is declared as a virtual body (similar to rudder and propeller). This virtual body is connected to the hull with a rigid connection.

3.5.3 Adaptive Grid Refinement

Adaptive grid refinement has been used for both grids. To capture the free surface accurately, the criterion used for both the grids is the free-surface tensor. To conserve the boundary layer only longitudinal refinement is enable. The parameters used for AGR are shown in table 3.11. As the free surface cells in hull domain will not be aligned with the background when the hull rotates (due to rigid motion of hull grid), the AGR is used more frequently and a lower refinement threshold is used in CG1. The extents of where AGR is applicable is shown in figure 3.12.

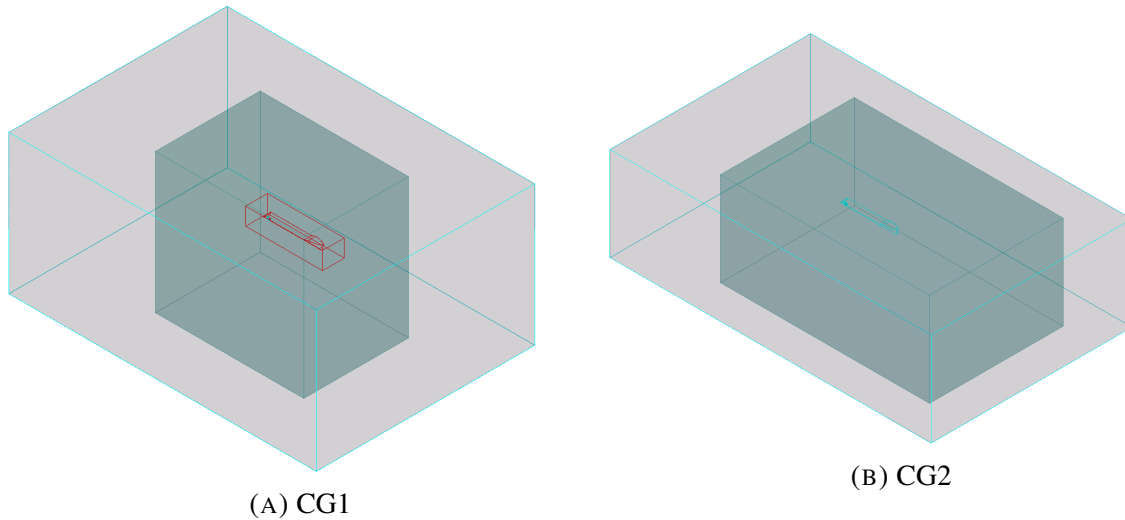


FIGURE 3.12. AGR extents (X and Y in Blue, Z in pink)

Parameter	CG1	CG2
Threshold (m)	0.0042	0.007
Buffer Layers (full)	4	6
Buffer Layer (fraction)	1	4
fraction for buffer layers	0.8	0.8
Steps between refinement	2	10
Max cells per partition	600000	1600000

TABLE 3.11. Parameter for AGR

3.5.4 Velocity Ramping

In order to avoid generating high amplitude waves, the velocity of the vessel should be increased gradually over a length equal to 2 times the ship length to reach the target velocity. The velocity ramp used in the 2 grids(CG1 & CG2) is a half sinusoidal ramp (see figure 3.13). Accordingly, the ramp is set to reach the target velocity of 2.00636 m/s in 12 seconds.

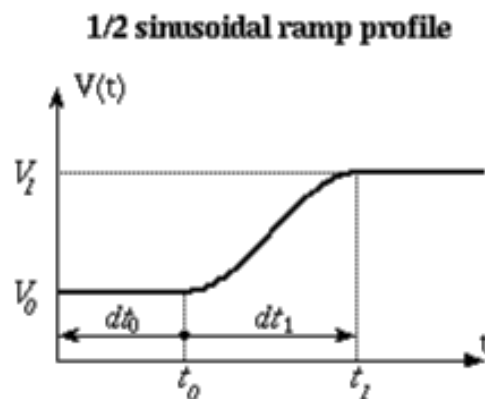


FIGURE 3.13. Half Sinusoidal Velocity Ramp

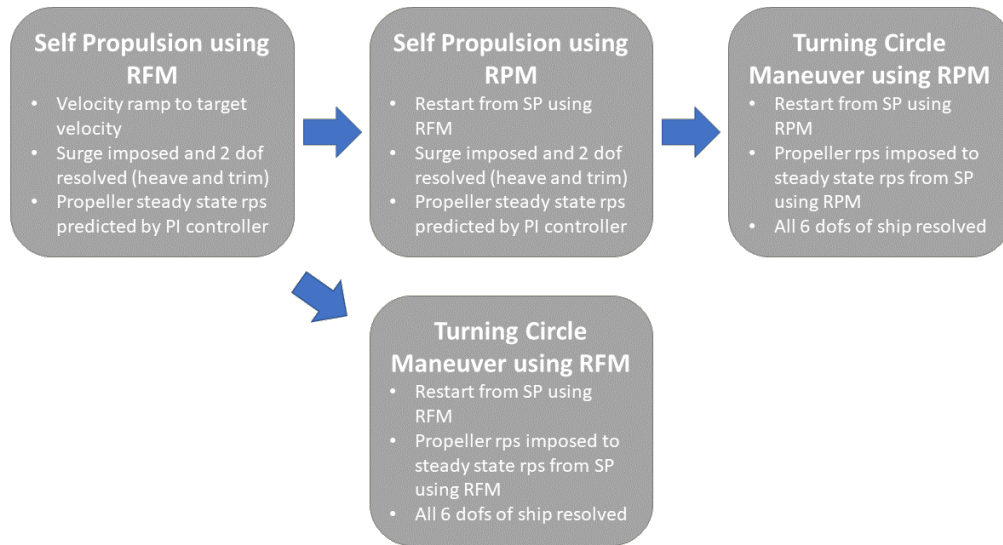


FIGURE 3.14. Simulation Workflow

3.5.5 General Work Flow

To determine the rps of the propeller required to maintain the target velocity the Self-propulsion simulation is performed. The rps for the self-propulsion is then imposed in the turning circle simulation. The self-propulsion simulation is performed using 2 methods:

- Rotating Frame Method (RFM) where the propeller is not rotated, but the domain momentum equation as mentioned in the previous section related to RFM methodology.
- Resolved Propeller Method (RPM) where the propeller domain is rotated about its axis using the sliding grid implementation. The boundary of the propeller domain is assigned with sliding grid boundary condition to enforce the connectivity of the propeller domain with the hull domain.

As Resolved Propeller Method (RPM) requires a small time step, the Rotating Frame Method (RFM) is used for the velocity ramp. The RPM will be a restart of the RFM simulation in Self Propulsion. The general work flow for simulations performed are detailed in figure 3.14.

3.5.6 Self Propulsion

The Self-propulsion simulations are a 3 dof simulation with the surge motion imposed, and the trim and sinkage solved which are the main motions when the ship moves in a straight line. The propeller rps is predicted using a dynamic library PI controller based on force equalization. The

PI controller used has a disadvantage that it is only capable of predicting rps of the propeller from the resistance of the ship and thrust from the propeller. It does not consider the rudder resistance. But, given that the rudder resistance is less than 2 N (discussed in results), the converged rps of the propeller is considered to be reasonably accurate.

3.5.6.1 RFM simulation

A uniform time-step of $\Delta t = 1/100 \times \frac{L_{PP}}{v} = 0.025s$ for all the simulations using RFM method.

To use RFM method, it is necessary to explicitly declare that the propeller domain uses RFM so that the solver uses the modified equation instead of rotating the domain.

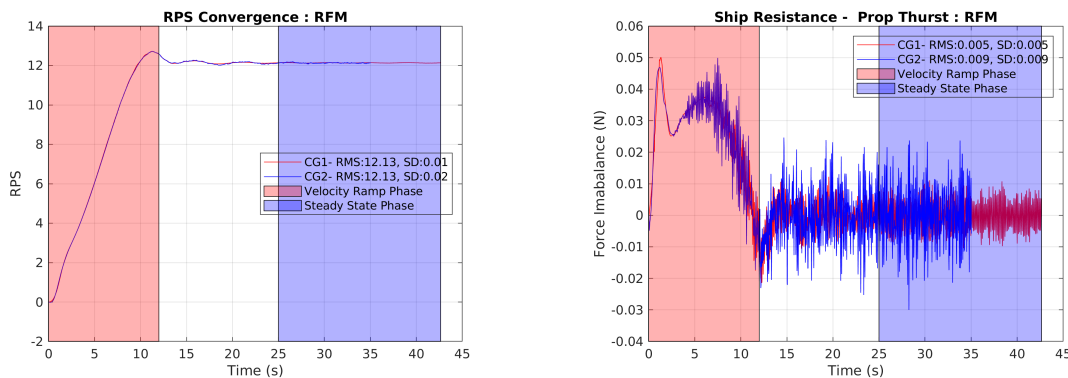


FIGURE 3.15. Converged of RPS using RFM

To fix the angle of the rudder, the rudder is assigned a constant angular modification of 0 deg/s.

The convergence of the rps for propeller and the force imbalance are plotted in figure: 3.15. Both grids converge to an rps of **12.13** with minimal fluctuations. The force imbalance is less than 0.01 N. The fluctuations in CG2 are higher than CG1 which implies that CG1 is a better grid which is because of aligned grids in CG1. The source of the higher fluctuations in CG2 is from rudder forces which will be discussed in Results Chapter. The converged rps obtained from this simulation will be used for turning circle RFM simulation.

3.5.6.2 RPM Simulation

The RPM simulation is a restart of the RFM simulation for a quick convergence. All the other settings are similar to RFM.

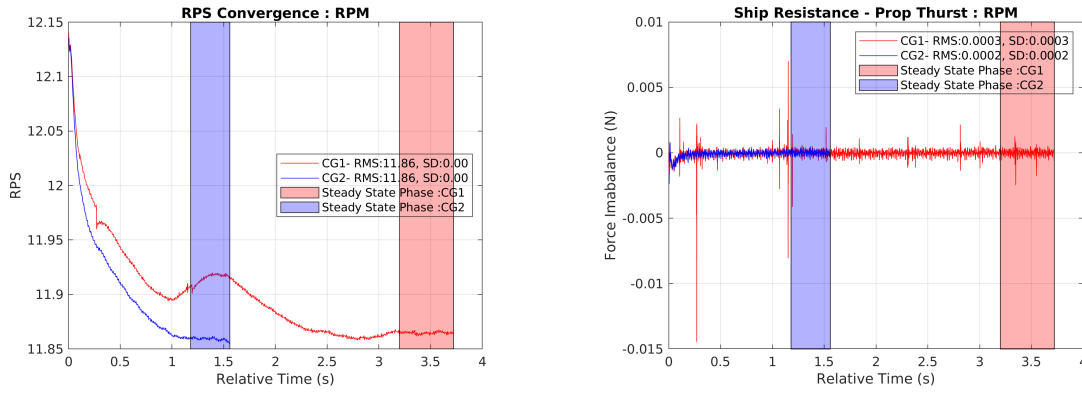


FIGURE 3.16. Convergence of Propeller RPS using RPM

In RPM method, the time step should be chosen such that the propeller rotates less than 2-3 degrees in each time step. From existing data we know that the propeller rps would be about 11.5 rps. In this regards the time step can be computed as

$$\text{Min } \Delta t = \frac{3}{\text{rps} \times 360} = 0.00072$$

The time step Δt is chosen as 0.006 s (2-3 degrees per time step) for CG1 and 0.004 s (less than 2 degrees per time step) for CG2. The reason for a higher time step in CG1 is due to an inherent fault in overset interpolation while will be discussed in the next section section.

Figure 3.16 shows the convergence of the rps conducted for CG1 and CG2 grids. Following the above, the steady state rps value for maintaining the velocity of 2.0006 m/s was found to be **11.86 rps**. The force imbalance of both the grids are less than 0.0005 showing better stability compared to RFM. Random occurrence of instabilities due overset interpolation (not of high magnitude) for CG1 can be observed in the Force imbalance Graph.

3.5.6.3 Setbacks and Trials

During the RPM simulations using CG1, high amplitude intermittent instabilities were observed. This is due to the inherent instabilities associated with the use of oversets. Several trials which are detailed below were conducted to overcome this problem:

- (1) **Trail 1 - Grid Alignment:** In the initial CG1 grid the background and hull grids were misaligned. After aligning the grid, though it was observed that the amplitude of fluctuations in RFM in steady state were lower, the instability in RPM simulations still occurred. A possible reason for this could be that even though the alignment of the

initial grid was ascertained, as the simulation progresses due to the rigid motion of the hull domain, the domain grids will not be aligned.

- (2) **Trail 2 - Hull Mesh refinement in propeller region:** As the instabilities were observed in the RPM simulations, the grid at the Hull-Propeller connection was investigated. It was also observed that when the instabilities occurred in predictions of X forces of the hull, instabilities in the propeller forces were also observed. The refinement zone including the rudder and propeller was further refined but maintaining the target size. Subsequent simulations did not yield better results.
- (3) **Trail 3 - Hull domain Free-surface zonal meshing:** The free surface was meshed as a zone with a height equal to the expected trim of the ship. This method helps to mitigate the misalignment of the free surface of the background mesh with the hull mesh when the ship begins to trim. This ensures refined cells at the free surface when the ship trims. The zonal mesh provides a better interpolation stencil at the free surface for the pressure gradient discontinuity. It worth mentioning here that adaptive grid refinement(AGR) does refine the free surface as the computation progresses but has a more localized effect. The free surface zonal mesh in tandem with AGR has shown better results by reducing the occurrences of the instabilities
- (4) **Trail 4 - Hull domain extent modification:** Adaptive grid refinement also refines the inter-grid boundaries. It is recommended that while using this algorithm, the overset domain boundaries have similar sized cells. This was ensured by extending boundaries of the hull domain was extended to avoid the effect of cell diffusion. The trial was not successful as instabilities were still observed in the RPM simulation.
- (5) **Trial 5 - Time step modification:** By running various simulations with different time steps it was observed that as the time step was reduced, the instability occurred faster. This may be attributed to increased probability of adverse alignment of the cells with time. With a marginally higher time-step, the occurrences of instabilities could be reduced to a great extent. The simulation conducted with a time-step 0.006 s did not show instances of instability. But it should be noted that such instabilities could arise if the simulation was continued further.

3.5.7 Turning Circle

In the turning circle simulation the rudder is rotated to an angle of 35 degrees starboard with a turning rate of 2.32 deg/s. Accordingly, the rudder is rotated to an angle of 35 degrees in 2.472 seconds using a similar angular ramp similar to velocity ramp.

3.5.7.1 Turning Circle using RFM

A 6 dof solved simulation is conducted for the turning circle simulation with a fixed propeller rps of 12.1 rps obtained for the self-propulsion simulation. This simulation is a restart of the Self Propulsion simulation using RFM.

3.5.7.2 Turning Circle using RPM

The setup of the turning circle simulation with RPM is similar to the simulation with RFM except that the simulation will be a restart of the Self Propulsion simulation using RPM and imposed rps of 11.86 for the propeller.

The high amplitude peaks caused due to overset interpolation in CG1 were observed during the simulation. The use of a lower order interpolation could create a better interpolation stencil and completely avoid instabilities. But as ISIS-CFD solves the dynamic pressure, a first order overset interpolation scheme will result in spurious velocity terms. The possible location and causes of the occurrences of the discontinuities were investigated and solutions proposed.

- The free surface: The free surface is a discontinuity for pressure gradient due to the change in fluid . The current implementation interpolates the velocity and the pressure at the free surface which could be one of the reason for such sudden peaks. A solution for this is to interpolate only the velocity and and solve for pressure.
- The boundaries of the ship domain: To avoid avoid adverse interpolation due to mis-alignment, a method was proposed. The interpolation between 2 grids are the worst when the grids are completely mis-aligned, i.e., the centroid of a cells at the boundary of the 1 grid lies on the plane of the face of the cell on the other grid. The solution to this problem is the use of AGR. The current AGR implementation refines the cell at the boundaries of domains and ascertains that the cell have similar size, but does not check the alignment of the cells. A check of misalignment and including an additional refinement at such zones could be a possible solution.

As these solutions proposed cannot be tested in the time-frame allotted to this project, the simulation for CG1 grid was continued ignoring the occurrence of the peaks. The effect of such peaks is discussed during the examinations of the results for the turning circle test.

RESULTS AND DISCUSSION

4.1 Self Propulsion

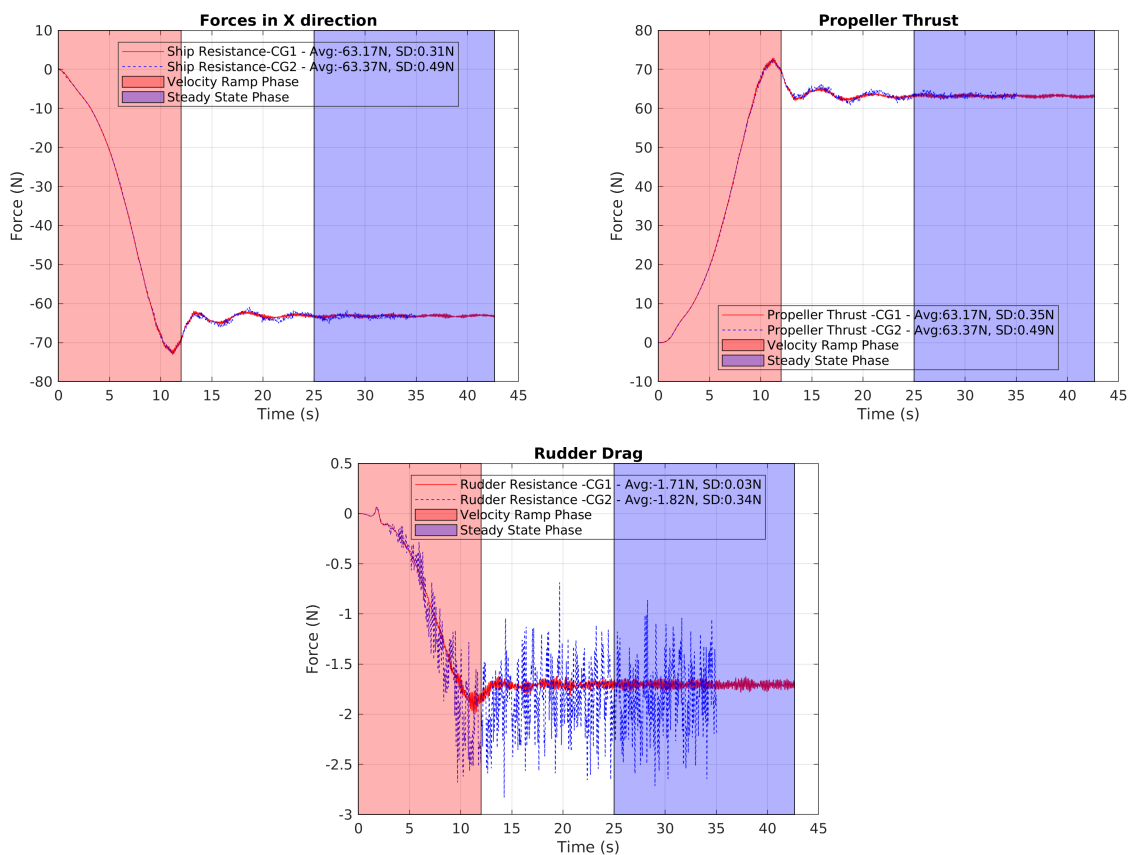


FIGURE 4.1. Converged of X forces using RFM

As the the analysis of the self propulsion concerns the steady state dofs and does not involve the comparison of trajectories, CG1 and CG2 generates similar results. The peaks due to interpolation errors in the transient phase of CG1 does not effect the steady state value.

It can be observed that CG1 has a better quality grid compared to CG2 from Figure 4.1. The rudder forces in CG2 has a higher oscillation compared to CG1 which is due to the misalignment

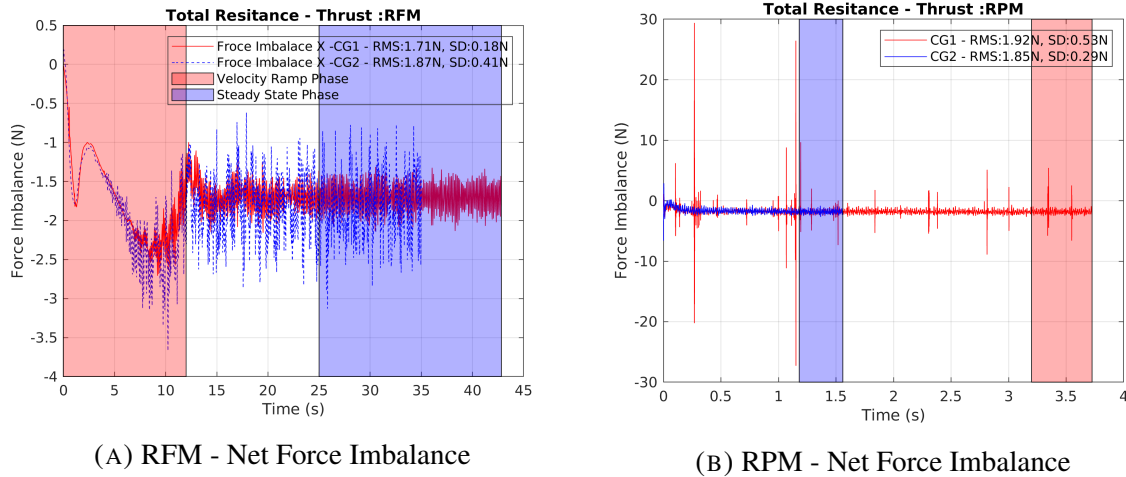


FIGURE 4.2. Force Difference at Stern

of the rudder grid and the hull grid. But the difference of the predicted rudder resistance is only of the order of 10^{-2}

In the section, the results of CG1 having better grid will be used to better assess the results predicted by the use of RFM and RPM.

4.1.1 Validation

The predictions computed using RFM and RPM are validated against the EFD results performed by IIHR for the same test case published by Kim 2020. In Ship motions predictions, RFM shows better results compared to RPM. This is attributed to the inability of the PI controller for propeller rps prediction to include the rudder resistance for force balance. As the rudder resistance has a small magnitude in comparison with the thrust and ship resistance (figure 4.2), the error in the prediction can be assumed to be minimal.

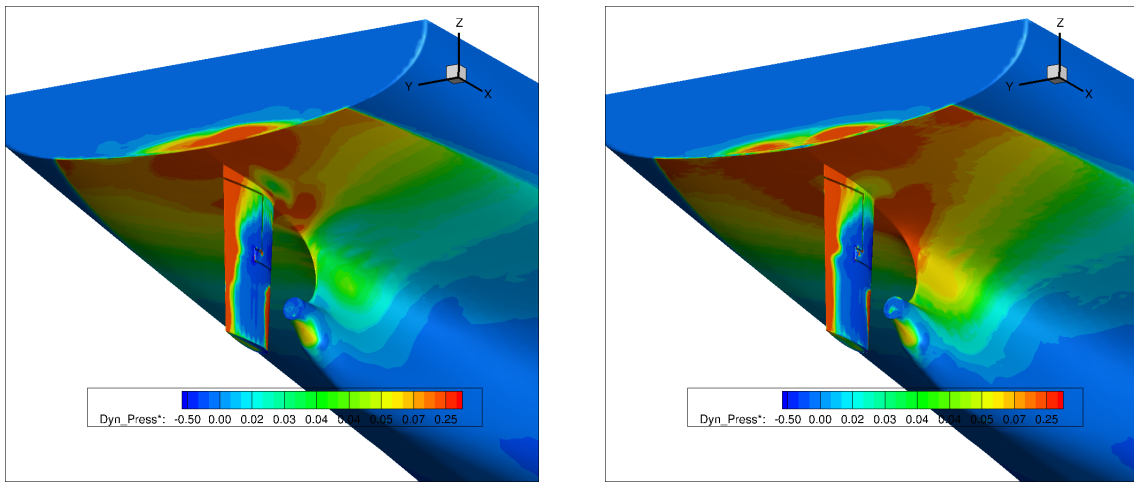
	IIHR	RFM		RPM	
	E Value	Value	E % Diff	Value	E % Diff
Ship Motion					
z/L	-0.0022	-0.00202	8.14%	-0.00200	9.19%
Roll (deg)	0.09	0.119	-37.73%	0.142	-57.59%
Propeller Characteristics					
K_T	0.245	0.2283	6.81%	0.2292	6.45%
K_Q	0.0397	0.03922	1.20%	0.03941	0.73%
n'	37.72	36.70	2.71%	35.88	4.87%

TABLE 4.1. Self Propulsion results validation

The sinkage predicted by both methods show a deviation of $<10\%$ when compared to EFD results with more accurate result predicted by RFM (8.14%) and RPM with a marginally higher

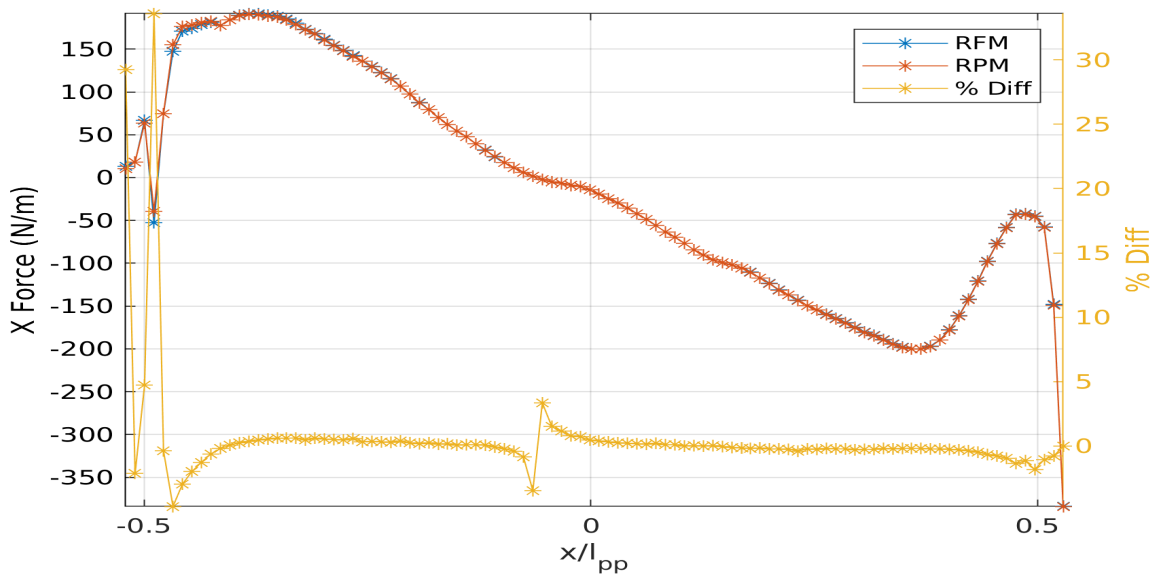
prediction(9.19%). The trim angle predicted by both methods show a notable percentage deviation from EFD results but the relative deviation is 10^{-2} . As the velocity of the ship is imposed, the difference in prediction by both methods are only due to the variation of pressure(viscous effects in the X direction is negligible compared to pressure) at the stern of the ship which can be observed in figure 4.3.

For assessing the propeller characteristics, the thrust coefficient, the torque coefficient and the non-dimensional rps (n') of the propeller have been used. In general, the propeller characteristics are well predicted by both methods with RPM showing better results. All the results are under predicted by both methods, which is caused by the problem of the PI controller previously discussed.



(A) RFM - Non-dimensional Dynamic Pressure

(B) RPM - Non-dimensional Dynamic Pressure



(C) X Force distribution along ship length

FIGURE 4.3. Force and Pressure Difference at Stern

4.1.2 Free Surface elevation

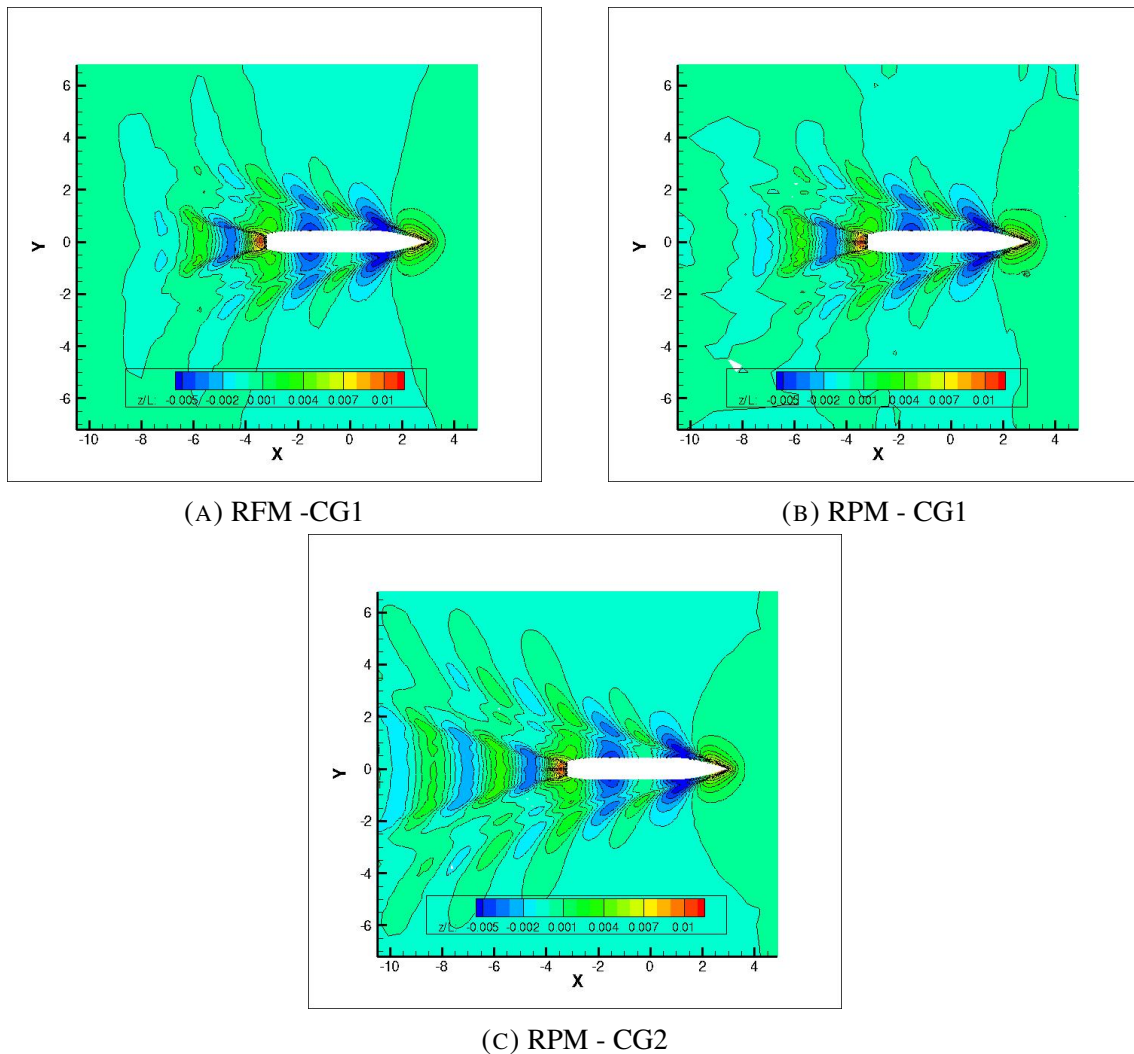


FIGURE 4.4. Free Surface elevation in Self Propulsion

The free surface elevation predicted by both methods are similar where the kelvin pattern is clearly visible as a set of divergent and transverse waves. Both the methods show identical predictions except in the aft center-line of the ship. The effect of the wake of the propeller and the rudder causes a localised elevation at aft of the ship along the center line in the RPM method while in the RFM method such a phenomenon is not observed. This is caused due to the difference in the flow modification by the rudder and propeller by the two methods which will be discussed in the next section. It can also be observed that the kelvin pattern extends well toward the aft in CG2 while the pattern is curtailed at a distance of $L_{pp}/2$ in CG2 simulations. As the Hull is meshed into the background in CG2, the diffusion of the cell size is continuous and extends beyond the size of the hull domain defined in CG1. So, as the cell sizes are large at the boundaries of the hull domain and background domain of CG1, the numerical attenuation is higher and the wave generated by the ship diffuses rapidly in comparison with CG2.

4.1.3 Wake Flow

The locations of the sections used to assess the wake flow are shown in figure 4.5 for CG1. The influence of the direction of rotation of the propeller on the flow is investigated.

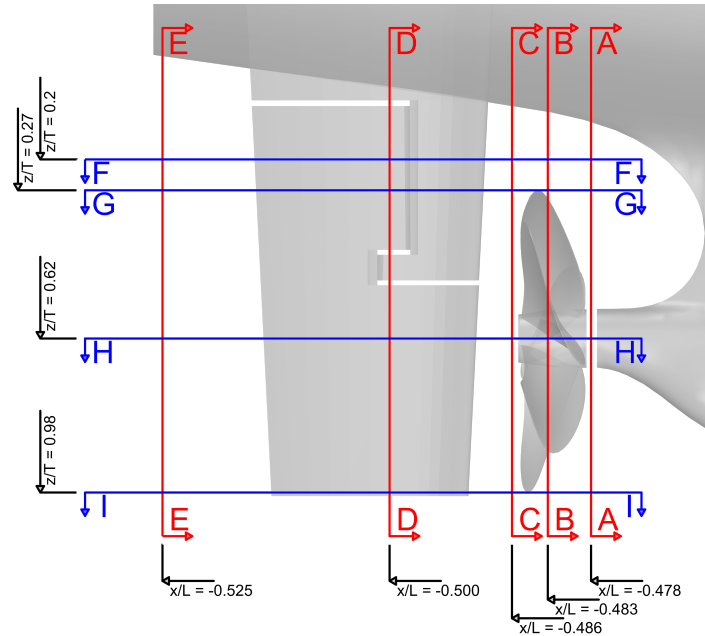
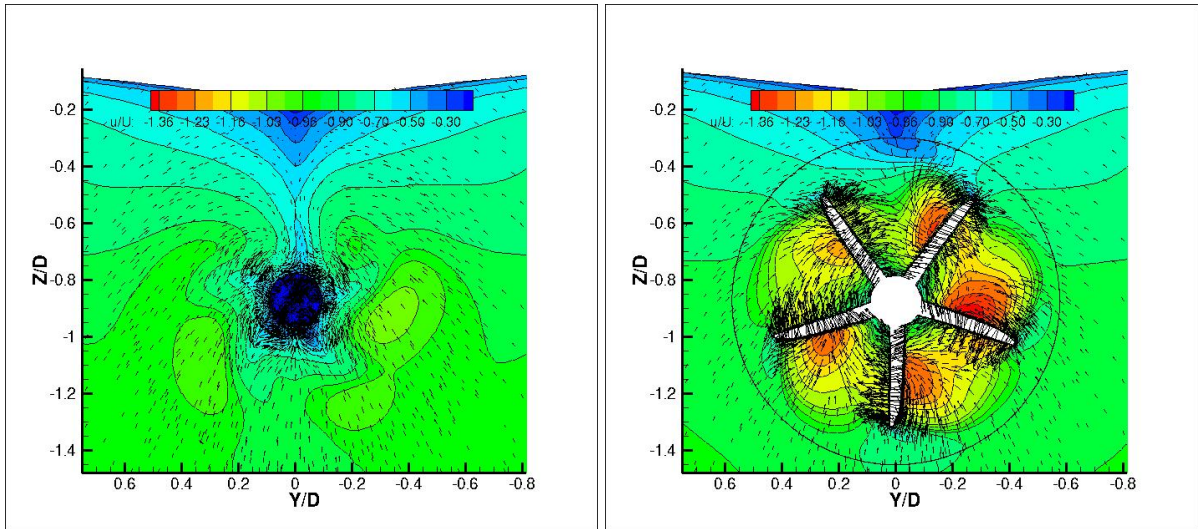


FIGURE 4.5. Sections used to wake analysis

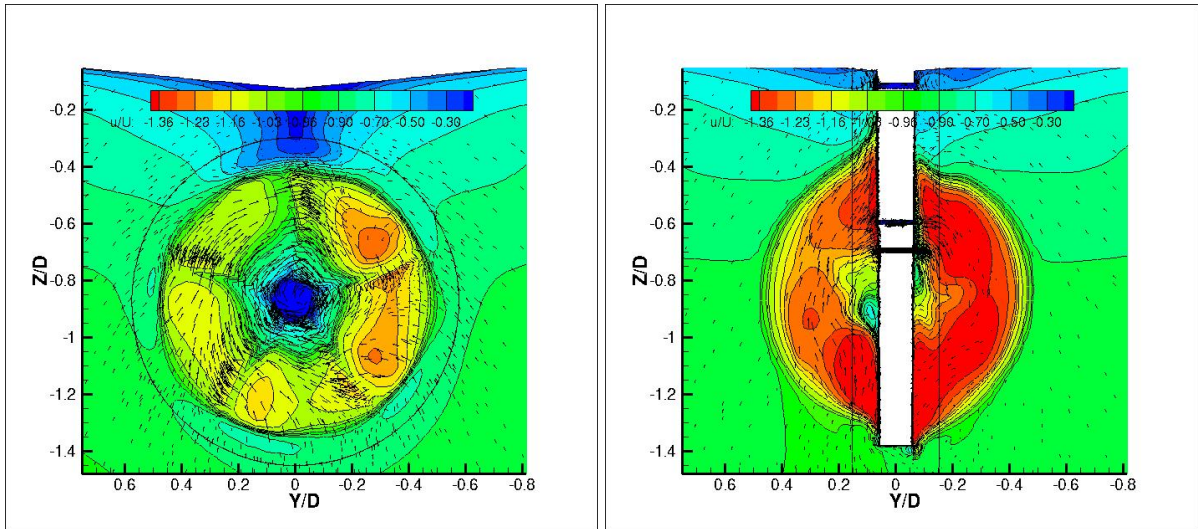
The propeller inflow (figure 4.6a) predicted by the RPM method shows a marginally higher axial velocity on the starboard side. The axial velocity at the root of the propeller blades is close to zero. The velocity gradually increases till the mid span of the blade where the suction by the propeller is the highest and later a uniform velocity distribution is observed. The lateral and vertical velocities show the flow moving towards the center of the propeller. It is observed that the lower side of the propeller has a dominant vertical velocity while the v velocity is dominant between the hull and the propeller except close to the center line where the lateral velocity falls close to zero. The axial velocity trend at the center-line between the hull and the propeller has lower value than the ship speed with the velocity close to zero near the ship and gradually increasing towards the propeller caused by the flow detachment at the aft of the ship.

Section at the Propeller (figure 4.6b) clearly shows the axial velocity is higher at the starboard side of the propeller which implies that the starboard blades have a higher angle of attack compared to the port blades. The thrust is produced at mid span of the trailing edge where the flow separates from the propeller.



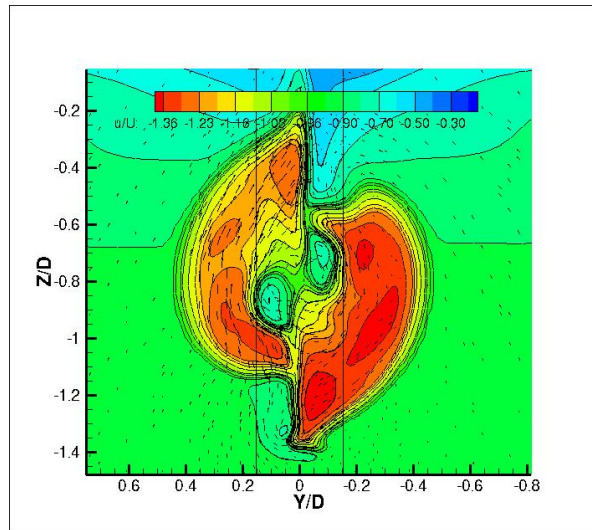
(A) Section A

(B) Section B



(C) Section C

(D) Section D



(E) Section E

FIGURE 4.6. Self Propulsion using RPM - Vertical Cut-planes

The resultant wake of the propeller (figure 4.6c) also shows a higher thrust on the starboard side of the propeller. The lateral velocities are observed to be circular with high tangential velocities in regions close to the trailing edge of the propeller blades. The section at the rudder (figure 4.6d) shows how the propeller wake interacts with the rudder. After the flow impacts the rudder, the axial velocity is observed to have increased on the port and starboard side. Since, the axial velocity is higher on the starboard side compared to the port, a net force towards starboard and a yaw moment turning the ship toward the port acts on the rudder. Since the simulation does not solve the sway and yaw dofs, this change in direction cannot be observed. Due to the presence of the rudder, the flow on the port and starboard are segregated. As the port side has the upward component of the flow velocity of propeller wake flow, the flow starts to shift upwards. Similarly, the flow starts to shift downward on the starboard side. The wake of the rudder (figure 4.6e) shows that the port side flow has shifted further up and vice versa on the starboard and the two flows remain separate.

From the stream lines shown in figure 4.7, the moment generated at the rudder can be observed. At the section of the rudder stock close to the hull (figure 4.7d), there is high velocity on the port side and the stagnation point is on the port side. At the section close to the tip of the propeller, we observe that the angle of attack of the rudder is increased and the velocity the region of high velocity turbulent flow has increased on the port. At the propeller, a re-circulation zone is observed between the rudder and propeller and the stagnation point has shifted to the starboard side with higher flow on the same side. Also, the flow is turbulent flow with high axial velocities on either side of the rudder. At the section of the lower blade of the propeller, the starboard side is observed to have high axial velocity. The flow predicted by RFM (figure 4.8) shows a high contrast from flow predictions by RPM. The inflow of the propeller generated by the propeller creates zones of suction near the blades. The starboard side is observed to have a higher velocity on the starboard side with a magnitude greater than the RPM method. The lateral velocities follow a similar trend as the RPM method. The velocity at center-line between the hull and the propeller is close to the ship velocity unlike in RPM where it is close to zero. At the propeller, only the zones on the starboard are observed to have high axial velocities. Unlike in the RPM method where the axial velocity in the zone of low axial velocity at center-line gradually increases to the starboard side, RFM predicts no transition in the zone. The axial velocities at the boundaries of the propeller domain show a sudden change. A similar observation is also noted in the wake of the propeller where the region between the propeller domain boundaries and the propeller have higher velocities compared to the region outside the propeller domain which is not observed in

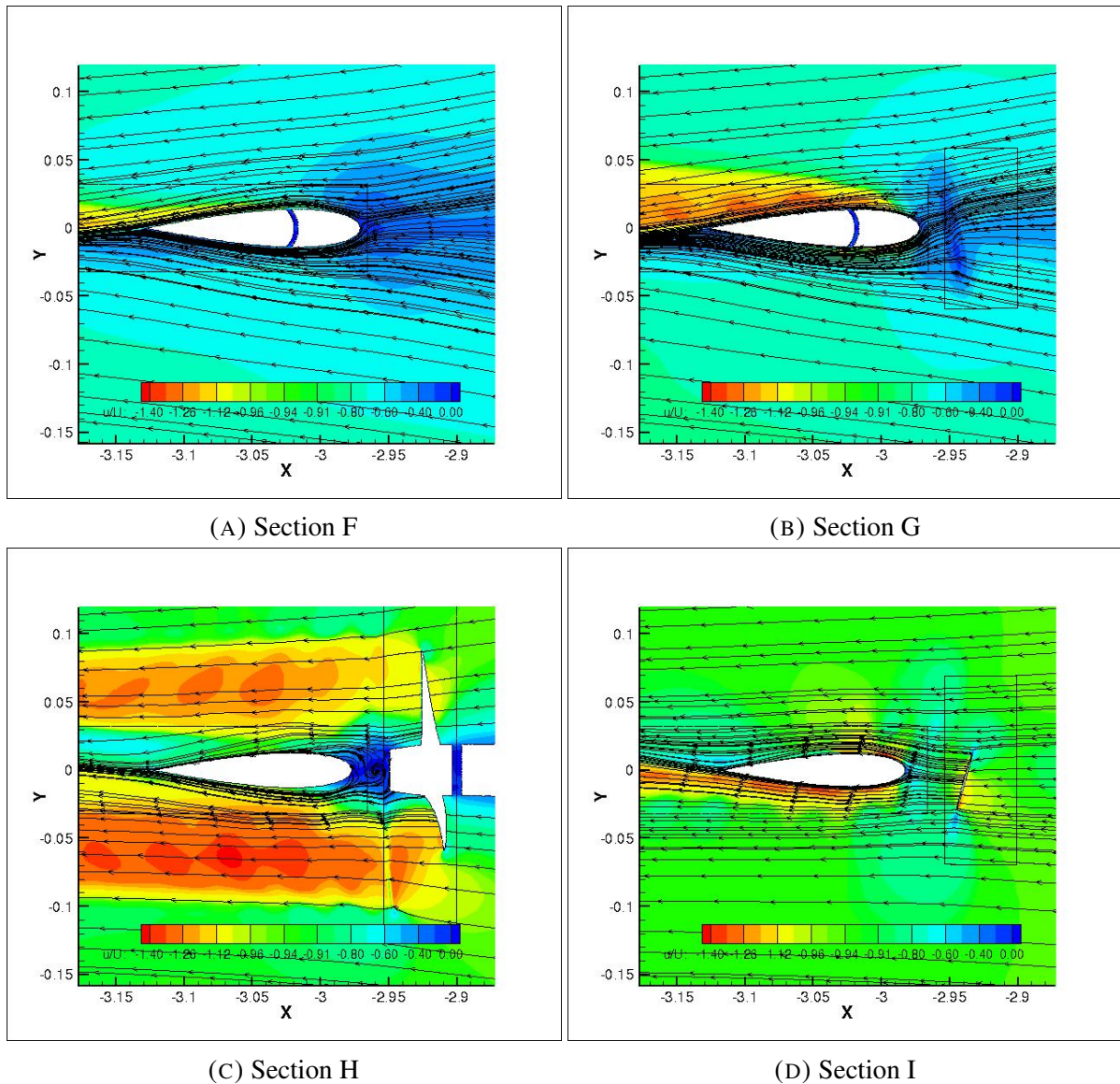


FIGURE 4.7. Self Propulsion using RPM- Horizontal cut-planes

RPM. The axial velocities in the propeller wake are high at the trailing edges of the top blades and the circular nature of lateral velocities is lesser in comparison to RPM method. After impact of the flow with the rudder, axial velocity distribution resembles the geometry of the propeller. The wake flow of the rudder show an arbitrary distribution of flow with mixing of the starboard and port flows.

The RFM method prediction at the section of the rudder stock (figure 4.8a) are similar to the RPM method. But the stagnation point shift to the starboard at the section at the top blade of the propeller unlike the RPM method where the shift takes place at the hub of the propeller. At the hub of the propeller the flow has generally a uniform flow of high axial velocity unlike RPM method where there were zones of high velocity in the flow. This shows that the flow

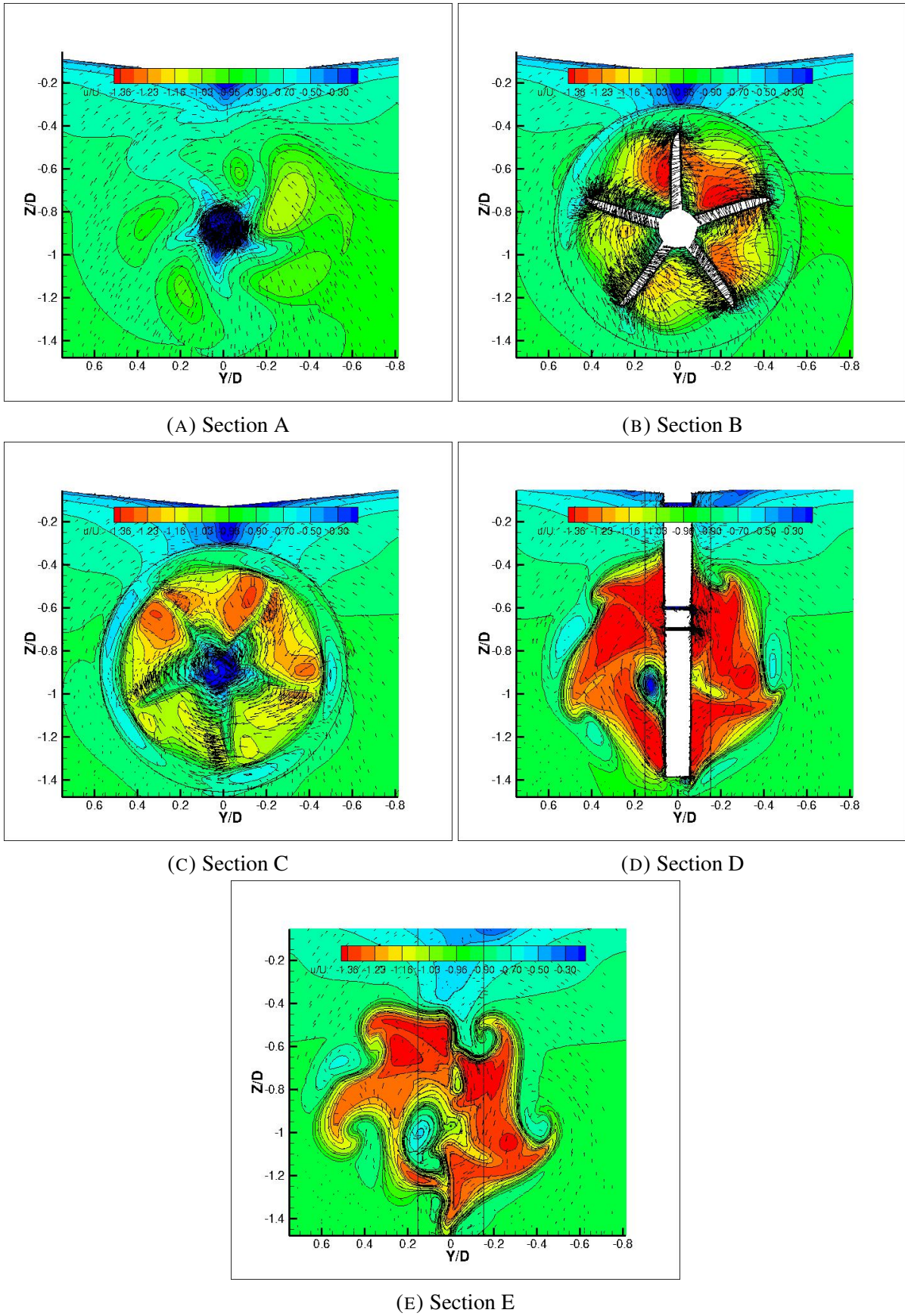


FIGURE 4.8. Self Propulsion using RPM - Vertical cut-planes

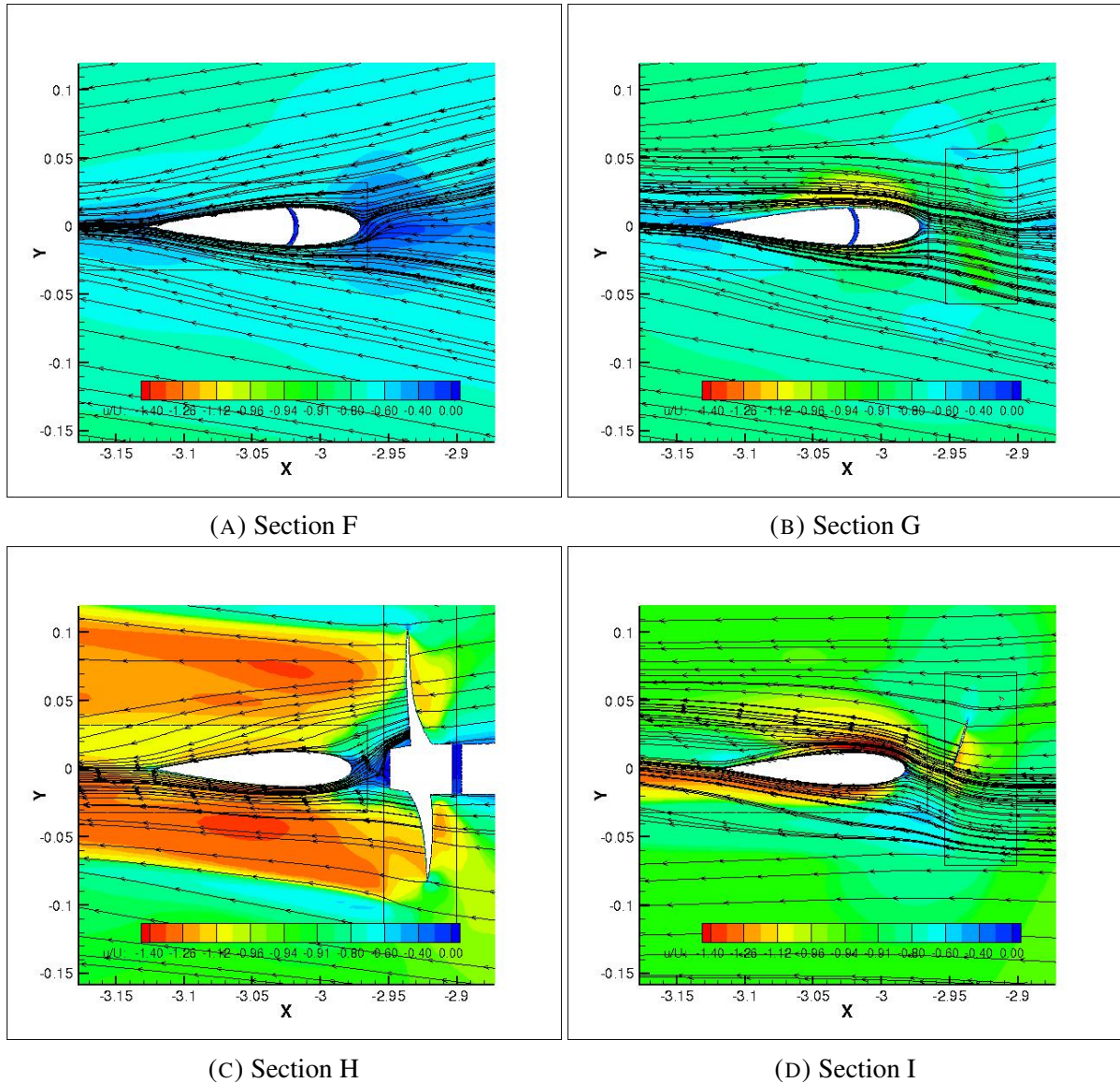


FIGURE 4.9. Self Propulsion using RFM- Horizontal cut-planes

generated by RFM has a lesser magnitude of circular lateral velocities. Also, though both methods predict lateral forces, the magnitude of the forces vary. The general angle of attack of the rudder predicted by RFM at each section is also higher compared to the RPM predictions. The flow predictions using RFM show an observable deviation from expected flow.

4.1.4 Vortical Structure Interaction

The vortical structures predicted by the RFM and RPM can be observed in figure 4.10. The figure shows the second invariant ($Q^* = Q * \frac{L_{pp}^2}{U^2}$) for the iso-surface at 1000 colored with the helicity (angle between the vorticity and flow velocity)

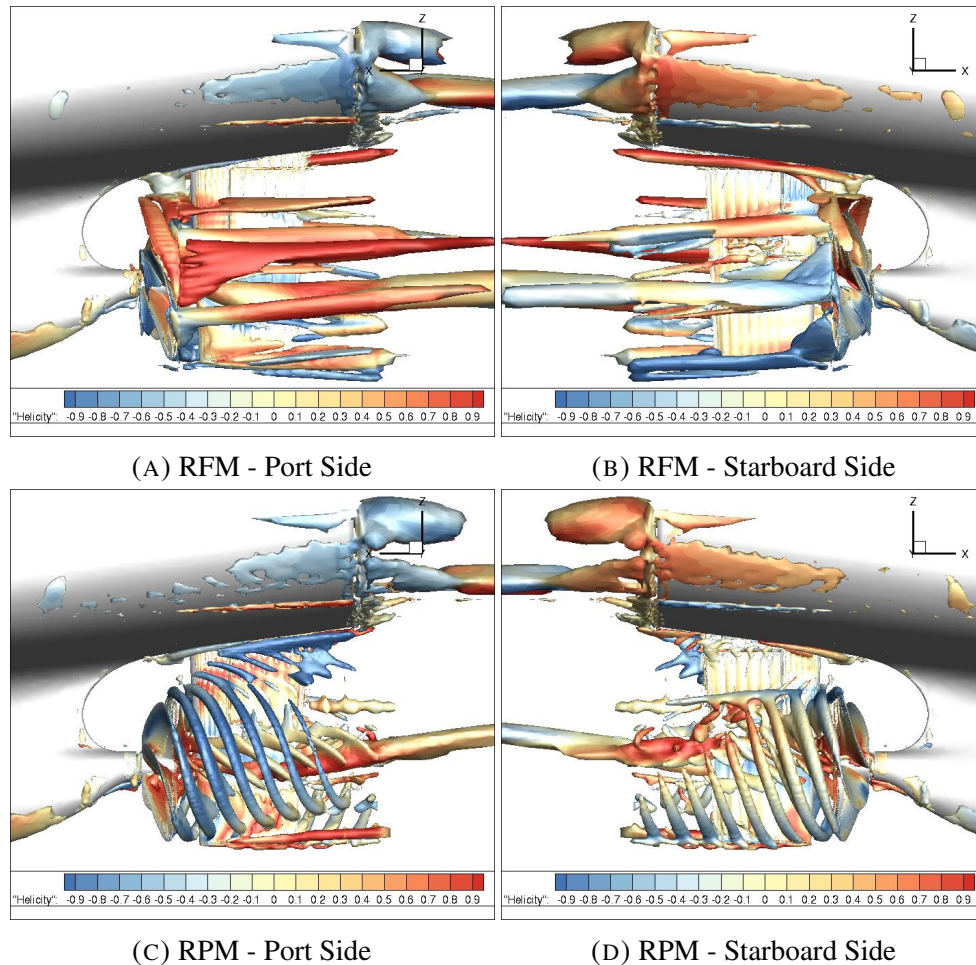


FIGURE 4.10. Helicity plot of Self Propulsion ($Q^*=1000$)

The RPM method shows a helical structure prediction which is closer to the expected flow. The vortical structures have two sources of origin: the tip of the blade and the trailing edge of the blade. The vortical structures originating from the tip of the blade have a rotation in the opposite direction of the flow velocity. The angle between the flow and the vortex are at 180 deg on the port and at almost 90 deg on the starboard side. This was observed in the previous section where the port side had higher lateral velocities and starboard had higher axial velocity. The vortices on the portside after interaction show a tendency to move toward the rudder stock maintaining the same angle with the flow due to the upward velocity component. The interaction at lower tip of the rudder on port side, show that the the vortex and flow velocity are in the same direction. On the starboard side the vortical structures after interaction show a tendency to move down and later the vortex direction aligns with the flow. The vortical structures generated at the trailing edge of the blade are closer to the hub. These structures have a rotation in the direction of flow. After interaction with the rudder, these vortices begins to diffuse.

The RFM method predicts straight line vortical structures. The trend is completely different from RPM. The port side show strong rotation in the direction of flow while the starboard side shows high rotation in opposite to the flow. The main source of vortices are from the tip of the blade. The vortex cores from propeller are appear to be in line with blades. This is due to the the static position of the propeller while using the RFM method. The contrast in vortex prediction can be observed in the absolute vorticity plot (figure 4.11) where RFM predictions show the vortex core gradually diffusing in the same plane as it moves away from the propeller while the RPM predictions show the helical motion of the vortex.

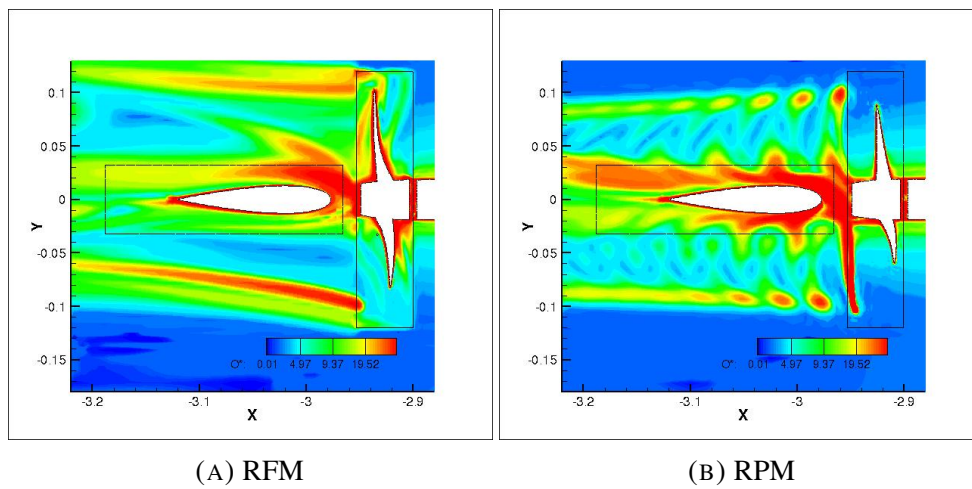


FIGURE 4.11. Non-dimensional absolute vorticity - Z section at Rudder Propeller

4.2 Turning Circle

Due to the exorbitant time requirement for RPM turning circle (amounting to close to 2 months in CPU time) time constraint imposed on the project, the simulation of the RPM simulation of CG1 has to be stopped prematurely before attaining steady state. The RPM simulation using CG2 attained steady state owing to the lesser requirement of adaptive grid refinement. The results mainly discussed in this section pertains to the RFM simulation conducted in CG1 and the RPM simulation using CG2. Where ever possible the results of RPM method for CG1 has been discussed.

4.2.1 Validation with EFD results

The predictions of RFM and RPM for the turning circle simulation are validated against the EFD results from MARIN published for the SIMMAN 2014 workshop. The EFD turning circle test was conducted for a 4 dof system (surge, sway, roll and yaw). In addition, the results are

compared with actuator disc (body force method) model simulated by Dr. Ganbo Deng from METHRIC team. The simulation with the actuator disc was conducted at the same scale as the simulations conducted in this work but the rps of the propeller is predicted to be **11.5** at model scale (lower compared to RPM). The non-dimensionalized trajectories predicted by the methods are shown in figure:4.12a. It is worth while to observe that though the instabilities in the CG1 using RPM has shown only marginal variations in velocity predictions, noticeable deviation in trajectory prediction is observed in comparison with CG2. So, in maneuvering simulations, where the transient region is important due to the relevance of trajectory predictions, the adverse influence of instabilities lead to a lesser accurate prediction.

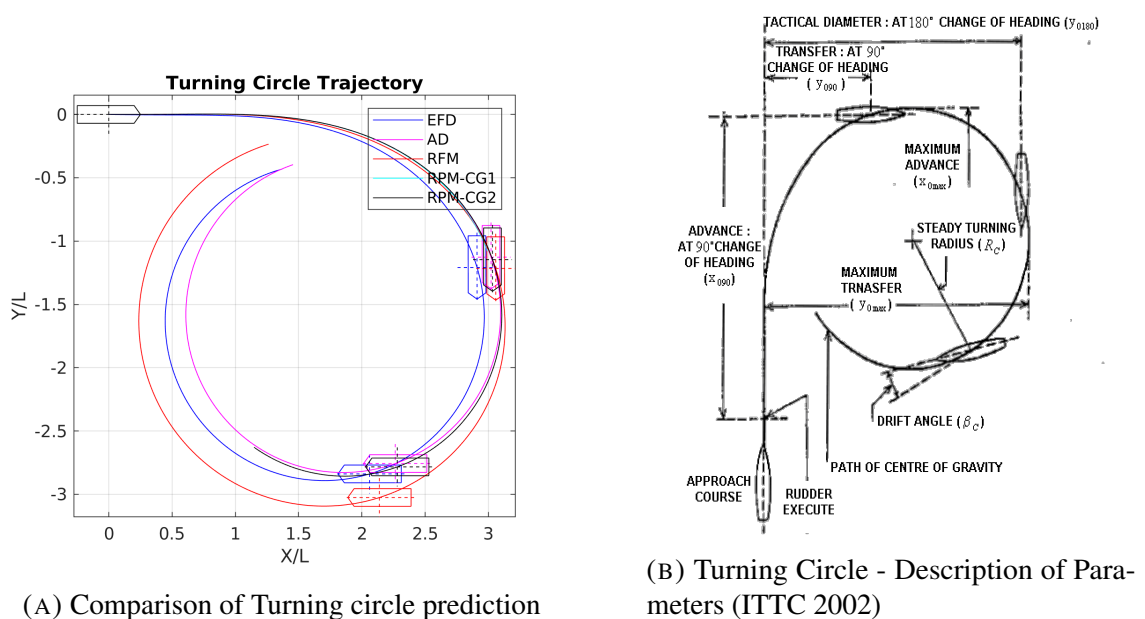


FIGURE 4.12. Turning Circle Simulation

In accordance with ITTC, the accuracy of the simulation is assessed using the tactical diameter, advance, transfer, final speed, time to change heading 90 degrees and time to change heading 180 degrees (refer figure: 4.16a). The comparison of the non-dimensional parameters are tabulated in table 4.2. The values expressed in the section follow the coordinate system of a moving frame centered at the origin of the ship and follows the surge, sway and yaw motion of the ship.

From table 4.2, the actuator disc and direct simulation show values closer to the EFD results with the predictions having an error of less than 5% except for the prediction of v velocity which are over-predicted by both methods with AP over predicting by 23% and RPM by 30.83%. RFM predictions are reasonably close to EFD values with an error less than 7% except for the velocity

	EFD	Actuator Disc		RFM (CG1)		RPM (CG2)	
		Value	E %diff	Value	E %diff	Value	E %diff
t_{90}	4.181	4.184	-0.09%	4.239	-1.40%	4.193	-0.28%
t_{180}	8.414	8.257	1.87%	8.486	-0.86%	8.080	3.97%
x_{180}	2.910	3.021	-3.81%	3.058	-5.08%	3.032	-4.19%
x_{max}	2.967	3.096	-4.35%	3.132	-5.55%	3.106	-4.66%
y_{180}	-2.839	-2.757	2.88%	-3.025	-6.57%	-2.783	1.95%
y_{max}	-2.892	-2.828	2.21%	-3.093	-6.97%	-2.856	1.21%
y_{90}	-1.208	-1.127	6.73%	-1.217	-0.67%	-1.147	5.13%
u	0.434	0.432	0.39%	0.494	-13.90%	0.442	-1.92%
v	0.120	0.148	-23.35%	0.155	-29.14%	0.157	-30.83%

TABLE 4.2. Result validation using ITTC recommendations

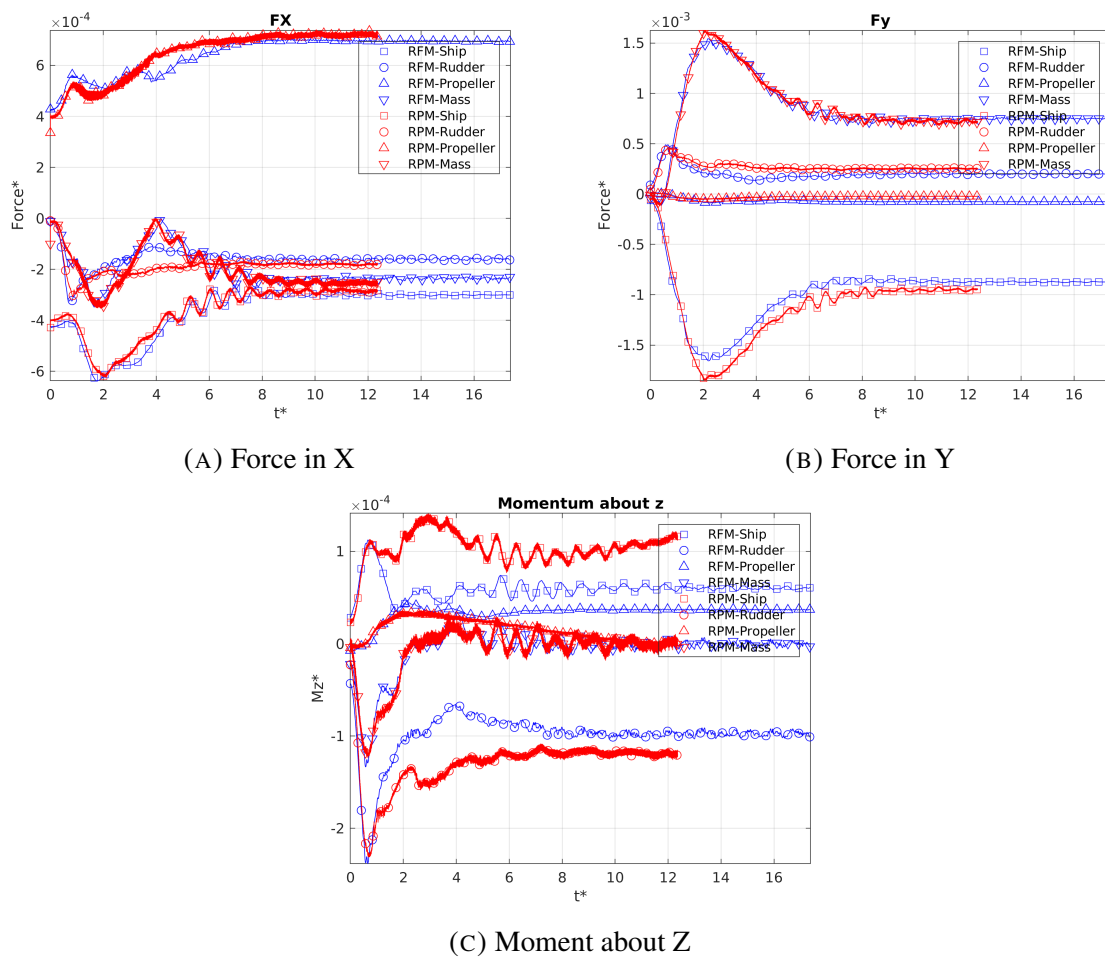


FIGURE 4.13. Forces and moments in the XY plane during Turning Circle

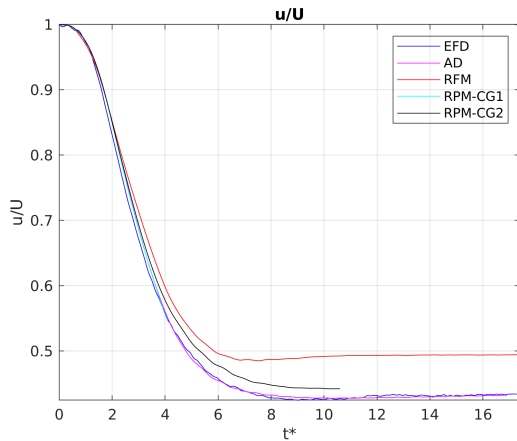
predictions which are over predicted, with u velocity over-predicted by 13.90% and v velocity by 29.14 %.

To understand the source of deviation of predictions from EFD data, an understanding of the physics of the turning circle is required. At the start of the simulation, the ship which is moving in x direction are subject to 3 main fluid forces, the drag caused by the hull and the rudder and the

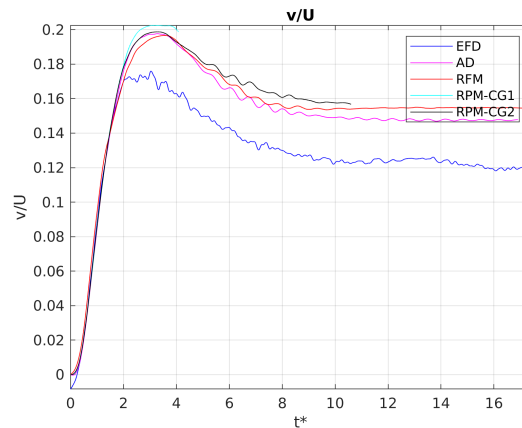
thrust by the propeller. The system is in equilibrium, i.e. the net positive force acts at the same point as the negative force in all 3 axis. Now as the simulation progresses, the imposed angular modification of the rudder toward the starboard cause a lift force toward the port side and a drag force. The lift force results in a moment at the aft turning the ship toward the starboard but also pushes the hull toward the port side resulting in a small displacement of the ship toward the port initially which can be observed in figure 4.12a. As the ship begins to turn starboard, the velocity which initially was in line with the ship(u), develops another perpendicular component(v) due to inertia. This can be interpreted as the ship starting to drift with an angle β made by the ship with the trajectory. When the ship drifts, it acts as a profile and is subject to a hydrodynamic lift force toward the starboard and a drag. The hydrodynamic lift creates a moment to oppose the moment by the rudder around the Z axis. In addition, the center of application of the net force of the hydrodynamic lift is below the water line while the force due to the mass of the ship is above the water line. This results in a positive roll moment about the x axis. The thrust produced by the propeller in line with the ship is modified due to the modification of the wake of the ship. The beta angle continues to increase till the system attains equilibrium. So, the main forces that are of concern in a turning circle simulation are in the XY plane.

The drift angle give a good understanding to the forces in the turning circle test. On comparing the drift angle in the stable regime (figure :4.14c) EFD shows a lower value in comparison to all 3 methods. We know that as the beta angle increases, the rudder lift and drag decreases (angle of attack of the rudder decreases) and the hydrodynamic lift and drag increases. From figure :4.13b, the hydrodynamic lift has higher magnitude in the Y direction compared to the rudder lift and is the dominating fluid force in the Y direction. So a higher β angle will result in a net force in the negative Y direction. To counter the hydrodynamic lift force, the body needs a higher centrifugal force thus resulting in a higher tangential velocity along the trajectory. As the sine component of the tangential velocity will have a higher effect of this force, the v velocities predictions by methods are higher in comparison with EFD (figure: 4.14b).

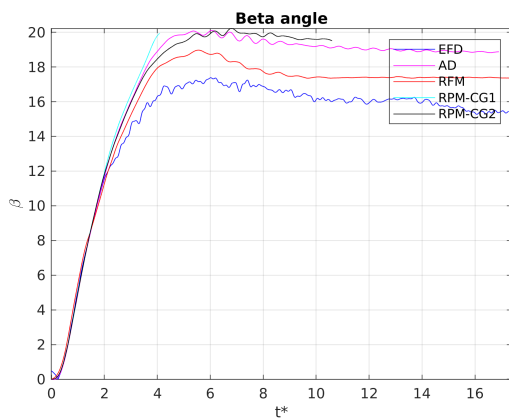
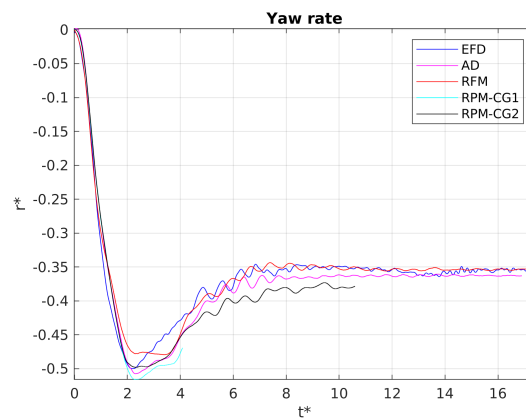
The u velocities predicted by AD and RPM are close to the EFD values. This is because the rudder drag and hydrodynamic drag are comparable in magnitude (figure 4.13b). As an increase in beta angle increases the hydrodynamic drag but reduces the rudder drag, the force in the X direction has a lesser effect for small changes in beta angle. The propeller thrust which is the balancing force against the hydrodynamic drag, rudder drag and the inertia, is only dependent on the wake flow generated by the hull. The higher u velocity for RPM can be attributed to the



(A) Non dimensional u velocity



(B) Non dimensional v velocity

(C) β in degrees

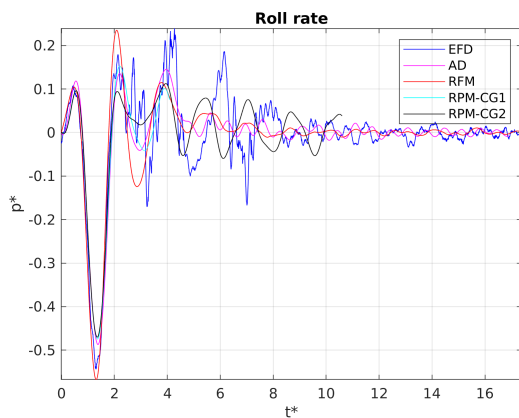
(D) Non-dimensional yaw rate

under prediction of the propeller thrust and the rudder drag. The lack of lateral rotational flow in the wake of the propeller as was observed in the Self-propulsion is the reason for the reduced drag prediction of the rudder. The AD simulation is observed to have a lower value compared to RPM method which could be attributed to lower rps used for the AD simulation which leads to a reduced thrust.

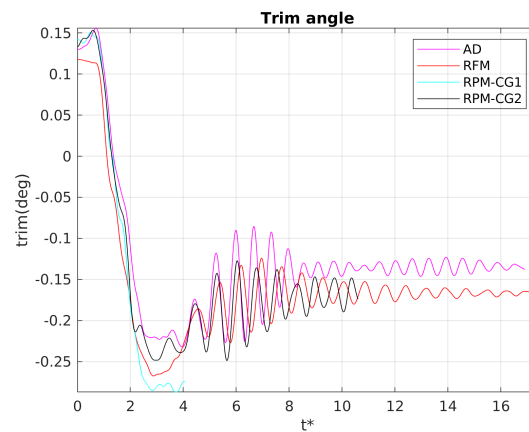
From the evolution of yaw rate with time, we observe that all methods follow almost a trend similar to EFD till attaining a peak value and predict the same value at steady state. The deviation in the trend can be observed between interval $t^*=2$ and $t^*=4$ where EFD follows a smooth transition to the steady state while the CFD methods show a local peak and later a smooth transition to steady state. The source of this could be traced to the hydrodynamic yaw moment (figure 4.13c) by the ship where a sudden increase in moment is observed at $t^*=2$. This is explained from the trim evolution plot (figure: 4.16b) where we can observe a similar trend as seen in the yaw rate. It can be observed that as the ship starts to turn starboard, the trim shifts from trim by forward to trim by aft. Between the time interval $t^*=2$ and $t^*=4$, the trim reaches a

critical point where the transom starts to immerse. This immersion of transom leads to a shift in the center of application of hydrodynamic forces acting on the ship towards the aft leading to an increase in momentum about z . So, the vessel, in order to attain steady state requires a higher drift angle.

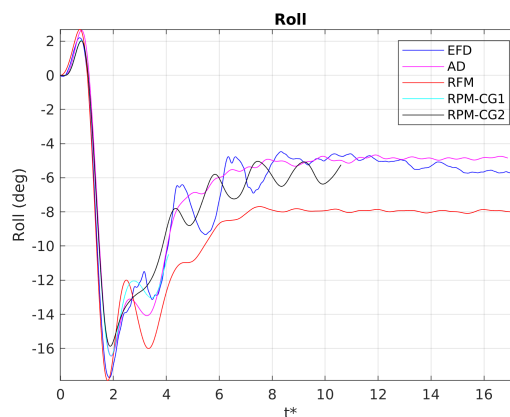
The EFD test which has only 4 free dofs and does not include the trim and sinkage. So the net hydrodynamic force on the hull will be more towards the forward in comparison with the 6 dof simulations conducted in this study resulting in a lesser drift angle. Thus, it is important to note that though the main forces concerned in the manoeuvring study are the forces in XY plane (and moment about Z), the inclusion of the sinkage and trim should be considered in complex geometries as the rigid body motion results in a modification the wetted surface area.



(A) Non dimensional roll rate



(B) Trim in degrees



(C) Roll in degrees

In the case of RFM simulations, the lower drift angle is a result of under-prediction of the rudder force and moment because of the less accurate prediction of flow from the propeller as was observed in the Self-Propulsion. The roll angle prediction by RFM also shows deviations from EFD data, while RPM and AD predictions are close to expected values

4.2.2 Free surface and Wake Flow

The predictions for free surface elevation using RFM are observed to vary from RPM (figure 4.16). The variation, as discussed in the previous section are mainly related to the the propeller flow leading to change in the drift angle prediction. The diverging waves on the port side create a sharper angle at the bow and vice versa with starboard due to the drift of the ship. The diverging waves appear to have a longer field compared to the port. This could be caused by the angular superposition of subsequent divergent waves and the circular motion of the vessel. So, in the frame fixed at a given time with reference to the ship, the diverging waves on the port side has an increasing u velocity while on the starboard side, the u velocity reduces.

The flow separation at the aft starboard side of the vessel is observed leading to a local zone of high wave elevation. The zone of flow separation is no longer at the transom of the vessel as observed in Self-Propulsion but extends from the transom till the beginning of the parallel middle body of the vessel. One of the possible reasons for this length of the zone is attribute to the sudden change in section area which in turn causes a discontinuity in the flow. It is interesting to observe that the zone length remains constant even for small changes in drift angle (RFM and RPM has predicted different drift angles but the zone length remains the same). But for higher drift angles, the zone of flow detachment will move beyond the beginning of the parallel middle body but the predictions of the zone length is highly dependent on the turbulence model used.

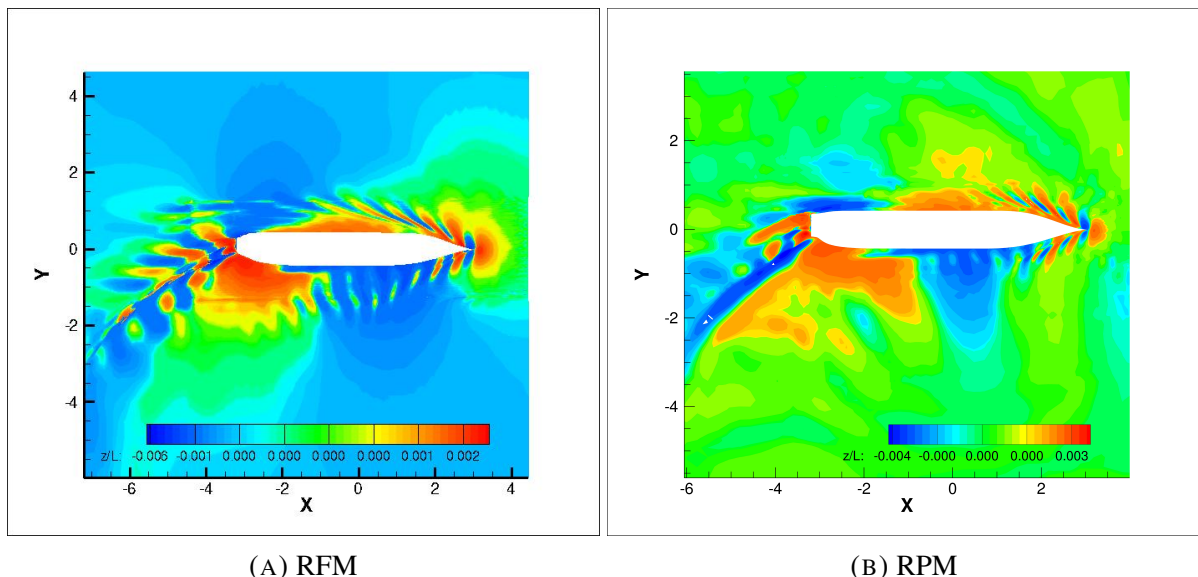


FIGURE 4.16. Free surface prediction

In the RFM method, discontinuities can be observed at the periphery of the hull domain (between $x=-4$ and $x=-2$). Such discontinuities exist across the hull domain boundaries. This discontinuities are mainly visible at the free-surface due to the sudden change in pressure gradient as mentioned

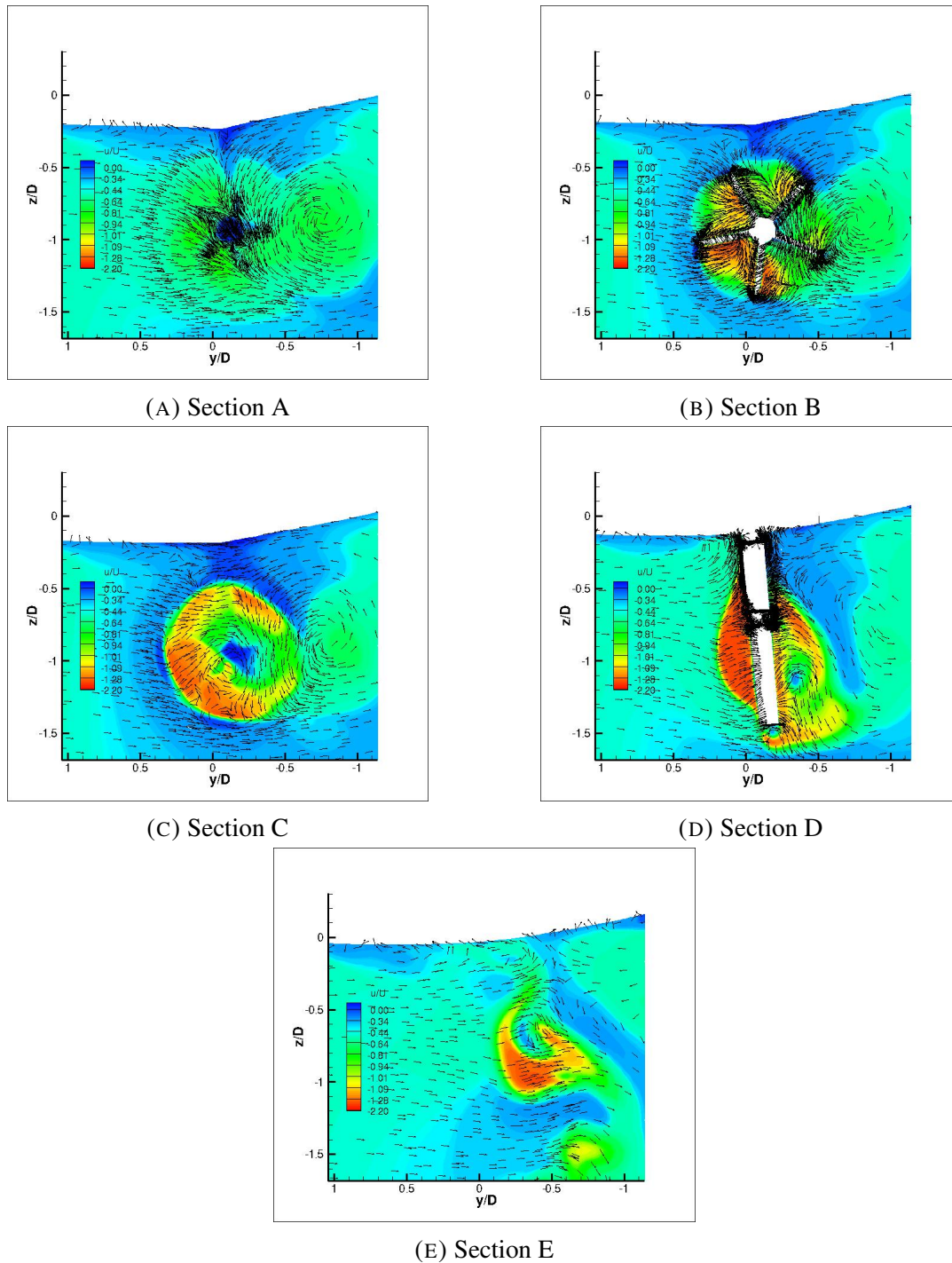


FIGURE 4.17. Turning Circle using RPM - Vertical cut-planes previously. These defects are more pronounced in the maneuvering simulation due to high roll angle leading to high angular misalignment of the hull domain with the background (6 dof free simulation). In the self propulsion simulation, though the trim dof was solved, the angle of trim is less than 0.1 deg and so the interpolation results were better comparatively.

The wake flow predictions of the two methods are analyzed at same sections as the Self-Propulsion Simulation (refer Figure 4.5). The RPM method flow prediction is shown in figure 4.19 and figure 4.20.

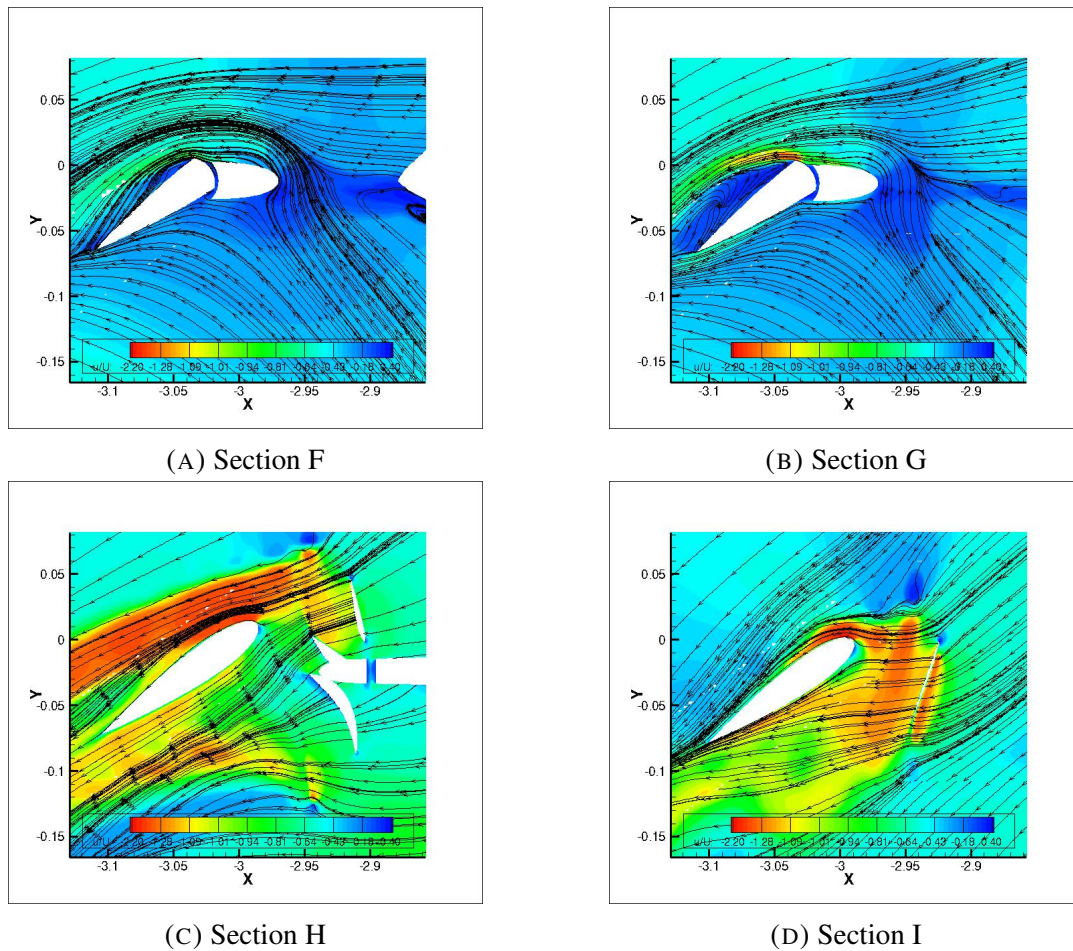


FIGURE 4.18. Turning Circle using RPM- Horizontal cut-planes

It is worthwhile to note that the velocities are relative to the ship and so show a net velocity toward the starboard as the ship has a net velocity toward the port side. Due to the constant lateral motion of the vessel toward the port side, all the sections show a higher axial velocity with circular lateral velocity toward the starboard side. In the region close to the propeller in the hull wake (figure 4.17a), due to the motion toward the port, the suction is higher on the port side blades in contrast with the self propulsion. Similarly, at the hub section of the propeller (figure 4.19a), the higher axial velocity flow are observed on the port section at the mid section of the propeller blades. subsequently the wake flow (figure 4.19b) on the propeller lower port side is observed to have high axial velocity. After the rudder interaction (figure 4.19c), the high velocity flow on the port side causes a pressure toward the port side resulting in the yaw moment from the the rudder. At the wake of the rudder (Figure 4.19d), the flow from the port and starboard of the rudder are observed to blend together and moves toward the starboard (relative to the ship).

The rudder stock (figure 4.18a and figure 4.18b) which is a fixed structure (does not rotate with the rudder) creates a yaw moment that increases as the β angle increases. But the effect of the yaw moment due to this appendage is insignificant compared to the yaw created by the rudder as the flow close to the rudder stock has a low velocity in comparison to the rudder which is subject to the high velocity flow from the propeller (figure 4.20a and figure 4.20b).

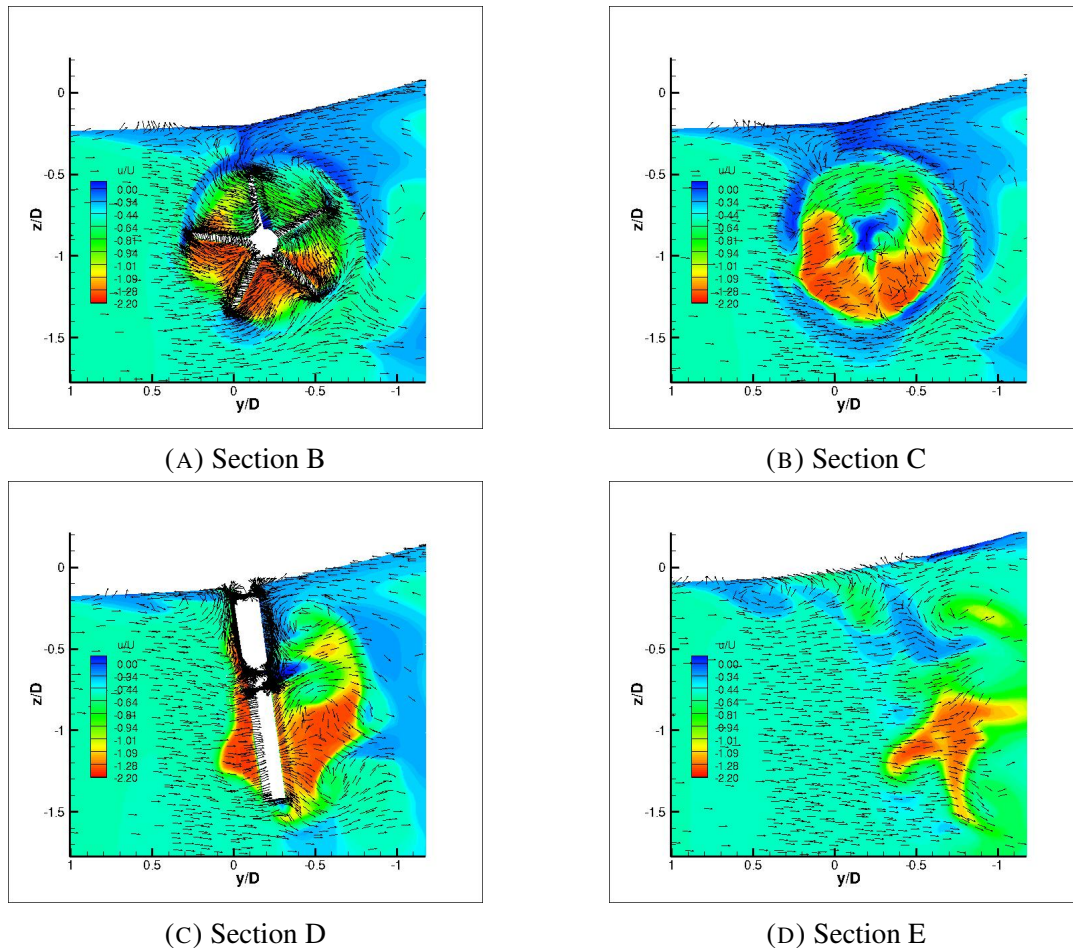


FIGURE 4.19. Turning Circle using RFM - Vertical cut-planes

The wake flow predictions using the RFM method show significant deviations from RPM. The sections shown are regions where the deviations can be observed distinctly. A marginally higher axial flow velocity is observed. This is caused due to the higher prediction of velocity of the ship. The high axial flow velocity of the is predicted at the lower half of the propeller in contrast with RPM predictions. The lateral flow has a lesser rotation which leads to a amorphous detached flow at the rudder. At the rudder, the port and the starboard side shows high axial velocity leading to a lower force on the rudder. The deviation of the beta angle from RPM results can be traced to the lower prediction of moment caused by the under prediction of lateral force.

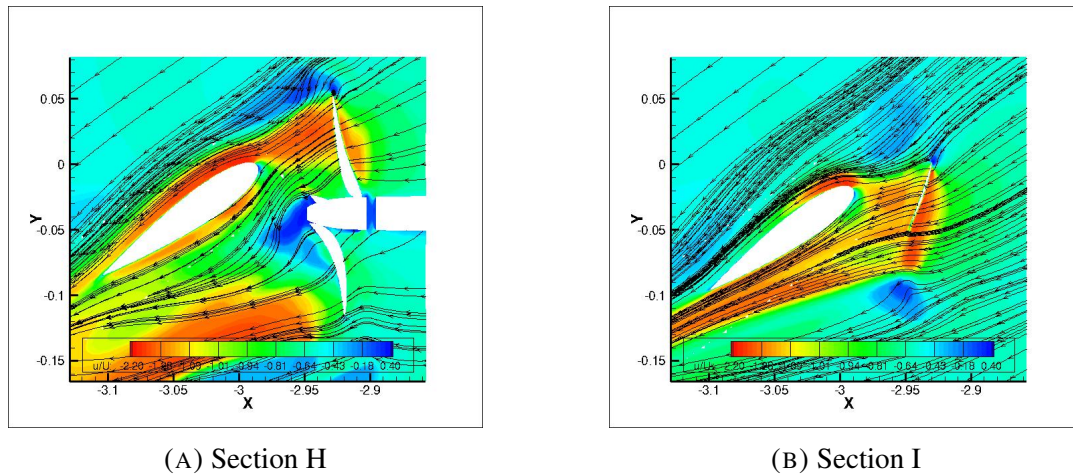


FIGURE 4.20. Turning Circle using RFM- Horizontal cut-planes

4.2.3 Vortical Structures

Figure 4.21 shows the second invariant plots for $Q^* = 1000$ colored by helicity for the 2 methods. As can be observed, the vortical structures are more complex compared to the self-propulsion simulation. In addition to the vortical structures from the propeller and the rudder, we can observe the vortical structures due to the flow detachment at the starboard of the ship and the transom. The vortical structures after the propeller-rudder interaction are in line with the rudder. The vortical structures predicted by RFM method are chaotic (figure:4.21a,4.21c,4.21e) and non-physical. Hence it is difficult to assess and shall not be discussed.

In the RPM method, the origin of the vortical structures are from the tip with rotation opposite to the flow velocity, the trailing edge of propeller blade with rotation in direction of flow (with a small angle) and the propeller hub similar to the self-propulsion simulation. After the interaction with the rudder, the starboard side the vortex is at 180 deg with the flow (in direction of propeller) while the on the port is vortex is in line with the flow (almost 0 deg). The propeller hub vortices after modification from the rudder have vortex at almost 180 deg with flow with the vortex intensification (the area of the iso surface reduces).

There are two vortical structures originating from two separate flow detachments due to the drift angle of the ship. One of the detachments occur at the starboard side due to the change in cross section of the hull and rotation is in direction of the flow. The other flow detachment originates from the bottom of the ship due to the flow from the port side. This flow move toward the starboard side by moving around the bottom of the hull. The flow detachment occurs at the

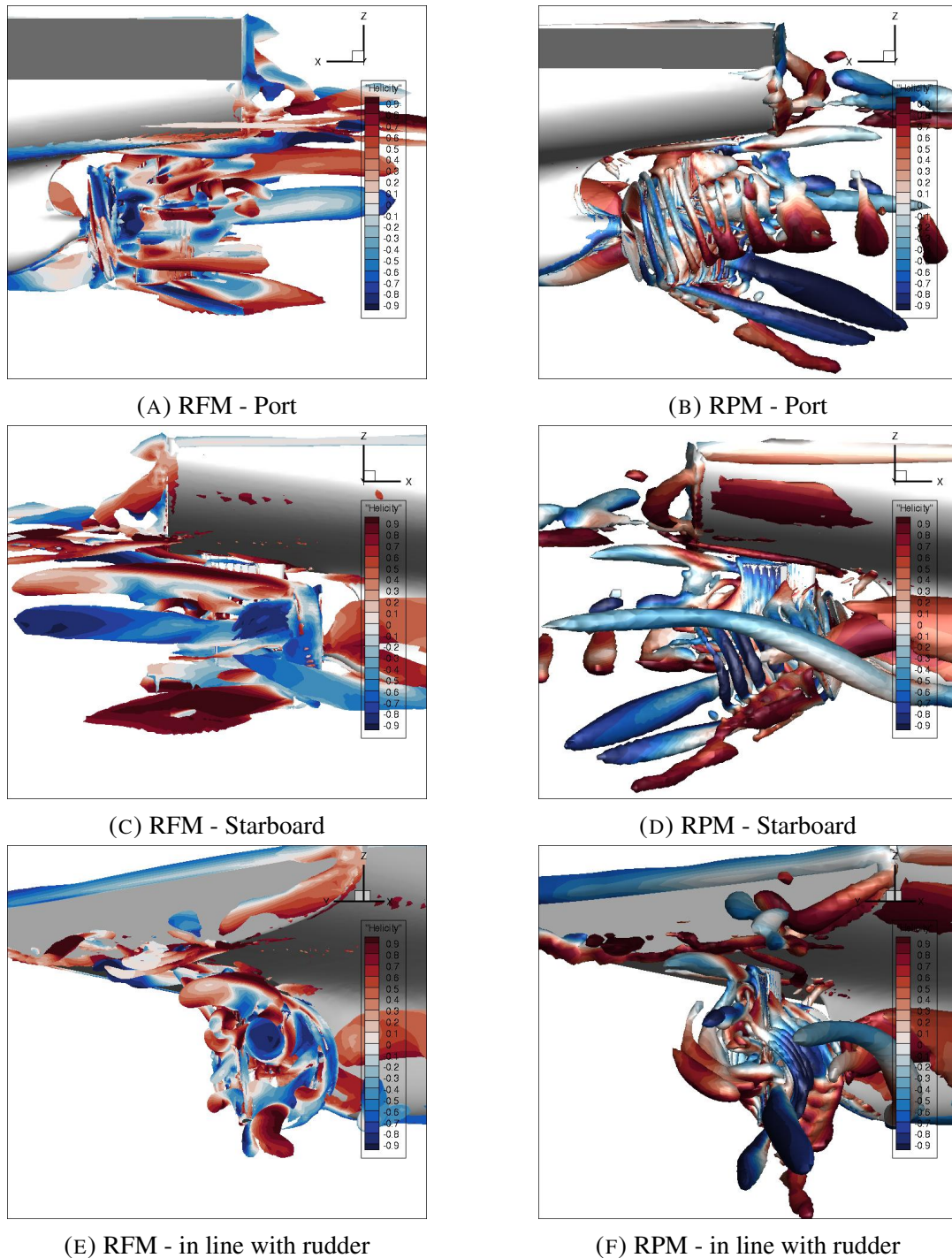


FIGURE 4.21. Turning Circle vortical structure predictions ($Q^*=1000$) bottom where there is a sharp change in geometry. The vortex has an angle of 90 deg at point of flow detachment with the flow and gradually increases and intensifies at the wake.

A intensity of helicity can also be observed at the transom in comparison with the Self-propulsion case. All the vortical structures show a net motion directed toward the starboard side caused due to the drift motion of the vessel.

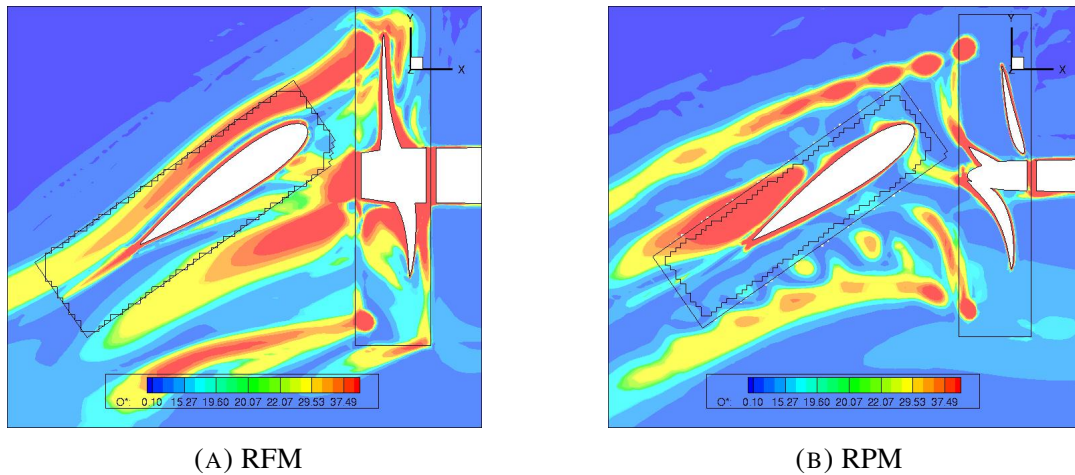


FIGURE 4.22. Non-dimensional Absolute Vorticity - Z plane Rudder Propeller Section in turning circle (CG1)

4.3 Mesh Analysis

Though the use of oversets lead to the loss of conservativeness of the system, it is in turning circle simulation to enable the relative motion of an rudder. During such relative motion of grids, it is necessary to maintain an acceptable interpolation stencil at the boundaries. Adaptive grid refinement has played a pivotal role in ensuring this by refining the cells at the inter-grid boundaries. This can be observed in figure 4.23. Though the use of the algorithm leads to isotropic property of the mesh, the interpolation is still acceptable as can be observed in the figure where the rudder grid boundary does not create a visible change in the propagation of the vortex cores.

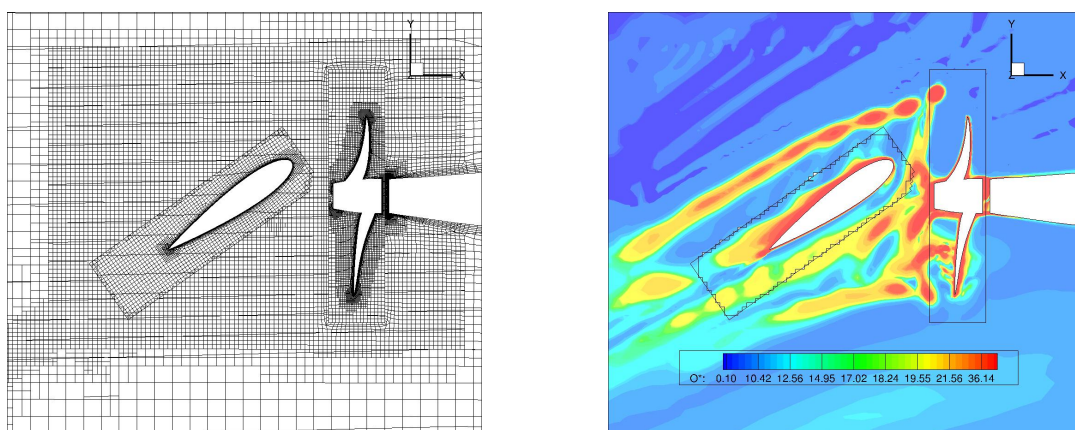


FIGURE 4.23. Free surface refinement - Z plane Rudder Propeller Section of CG1 in turning circle- Mesh (left) and Non-Dimensional Absolute Vortex(right)

The AGR has also been used for free surface capturing. This helps in avoiding the traditional method of meshing the wake as shown in figure 4.25. In addition, in CG1 due to the high roll of

the ship, the actual free surface is no longer inside the initial free surface zonal mesh. The AGR has inserted fine cells at the free surface thus enabling a more accurate result. It is worthwhile to observe that the AGR implemented also joins the cells where refinement is not necessary and so we can only observe fine cells at the free surface of the current time step. It is noteworthy that the discontinuities could not be avoided in the turning circle as a result of the free surface moving outside the free surface zonal mesh.

But the use of AGR increases the cost of computation significantly. This overtly observed during the turning circle simulation. In 1100 hours of computation, CG2 completed 3/4 of the circle while CG1 had not even completed 1/4 of the circle. This is mainly caused due to the selection of parameters. The AGR is more frequently used in CG1 and the threshold cell thickness in z direction is set to a smaller value. Though this setting is necessary CG1, the computational effort is increased by 3 times approximately in comparison with CG2.

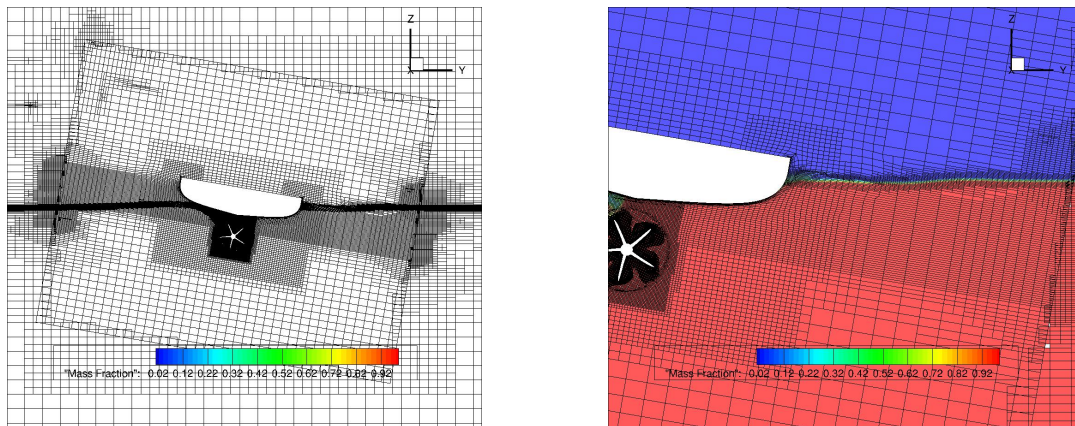


FIGURE 4.24. Free surface refinement - X plane Ship Propeller section of CG1 in turning circle- Mesh (left) and a zoom of mass fraction with mesh(right)

Though both CG1 and CG2 uses overset interpolation for rudder, interpolation errors occurred only in CG1. This is because the rudder is completely immersed in water unlike the ship and no overset interpolation occurs at the free surface where the pressure gradient is discontinuous in the rudder domain. In addition to the the pressure discontinuity difficulty, the interpolation at the free surface is further affected by the mis-alignment of cells which can be observed in figure 4.26. In the figure from self-propulsion, the cells at the intergrid boundary are of the same size but the edges of cells are not overlapping(best interpolation results) but lie along the centroid of the overlapping cell(worst interpolation results). The case is further worsened in the turning circle where a 3 angular mis-alignment occurs. The methodology of overset interpolation needs further investigation and with the current implementation, it is recommended to avoid the use of overset for bodies at free surface whenever possible.

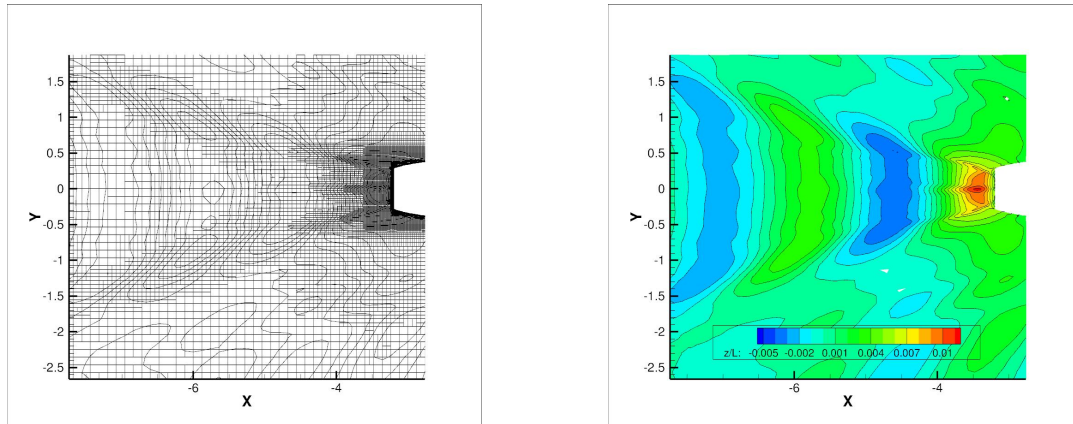


FIGURE 4.25. Intergrid refinement - X plane Ship Propeller section of CG2 in Self Propulsion- Mesh (left) and a zoom of mass fraction with mesh(right)

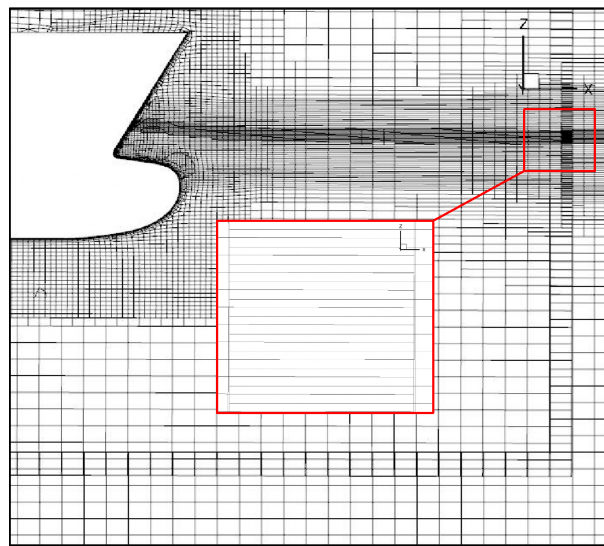


FIGURE 4.26. Mesh misalignment in CG1 (Self Propulsion) at the free surface intergrid boundary

A contrast of the vorticity predictions can be observed in figure 4.22. As was observed in Self-Propulsion, the RFM predictions of vorticity show the vortex cores moving in the same plane and diffusing as it moves away from the propeller. The vortices predicted by RPM show a helical trajectory. In addition, they show that the vortex core on the port and hub do not interact with the rudder while in RFM shows otherwise in the propeller plane.

It is interesting to observe the continuity of the vortex core as it passes through different domains showing a good overset interpolation resulting from good alignment between the domains in CG1 used for RFM. In CG2 observable discontinuities at the rudder- hull intergrid boundaries can be observed. The reason for better continuity in CG1 compared to CG2 is because the rudder domain and hull domain mesh in CG1 always has angular alignment in Y and Z while this is not the case for CG2 where a misalignment are in all the 3 axis.

CONCLUSION

In this study, the turning circle simulation of the KCS hull with modelled propeller and rudder using RFM and RPM methods were investigated. The solver used for the study is the ISIS-CFD solver. Two grids, one with ship (CG2) and background meshed together and the other with ship as an overset in the background (CG1), have been used for the simulations to assess the overset implementation used in the solver.

The prediction of the motion and propeller characteristics by RFM and RPM for self-propulsion were compared with the experimental data from IIHR and observed were within acceptable tolerance. The deviations are small, the source of deviations is mainly from the propeller rps PI controller's inability to include the rudder drag for its prediction. Flow assessment in the wake revealed a net yaw moment on the rudder. The effect of this moment was not observed as the motion of the vessel was restricted to a straight line. A study of the vortical structures revealed the source of vortices were from the, tip, leading edge and hub of the propeller.

The turning circle results were compared with CFD simulation with Acuator Disc and the MARIN EFD data. The AD and RPM method prediction were closer to the experimental results while the RFM predictions were marginally above 5% and with observable deviation in trajectory. The deviations of AD and RPM from EFD could be attributed to the difference in free dof's of the EFD and CFD. It was observed that, though the y moment and the z forces only play a small role in maneuvering of the vessel, the change of wetted surface area due to the trim and sinkage, were found to have an influence on the X and Y forces and Z moment in maneuvering simulations. Additional vortical structures were observed due to the flow detachment cause by the drift of the ship. The flow predicted by were non-physical and so the vortical structures were difficult to assess.

RFM method is a viable method for prediction of forces and moment of the propeller. But its inability to reproduce actual propeller wake flow makes it not suitable for trajectory prediction

in maneuvers. The trajectory predictions by AD inline with the experiments and is a feasible method for maneuvering prediction.

Direct simulation for maneuvers are highly expensive in terms of computational time and resources. The direct simulation of turning circle conducted in this study used over 1100 hours of computation time using 120 cores. So, direct simulation has limited to no application in the industry but such simulations give a good insight of the flow physics and are necessary in improving the understanding of complex flow and fluid-structure interactions.

Difficulties were faced during the use of CG1 grid due to instabilities in form of sudden peak forces with extremely high magnitude. These peaks lead to a marginally higher prediction in turning circle simulation compared to CG2. These peaks were due to the errors in overset interpolation at the overset domain boundaries due to grid misalignment and free surface due to the discontinuity in the pressure gradient.

Overset are a powerful tool in CFD and are the only viable method to simulate large body displacement relative to the domains. But it comes with their own dis-advantages. The primary disadvantage is the loss of conservation of the system due to the use of interpolation. The use of overset could also leads to errors in interpolation caused by the misalignment of grids. Adaptive grid refinement plays a crucial role in mitigating this problem by creating a acceptable interpolation stencil throughout the simulation especially at the free surface and domain boundaries. But such algorithms increases the computation time as was observed in this study. Hence, the use of oversets should be avoided whenever possible, but when used, the parameters of adaptive grid refinement should be set optimally to avoid unnecessary increase in computation time.

5.1 Future outlook

- The use of RFM for predictions needs to re-checked using a better selection of the time-step based on the number of blades. Choosing a time-step such that a blade rotates to the position of the adjacent blade could yield better results as the blade-fluid interaction errors could be minimised.
- The current study deals are conducted at calm sea condition. It would be interesting to study the flows generated in the case of waves using direct simulation and actuator disc.
- Adaptive grid refinement: Improvements in boundary refinement could help avoid cases of bad interpolation stencil.

- **Overset implementation:** The current overset implementation causes discontinuities at especially at the free surface due to the discontinuity of the pressure gradient. A more robust implementation of interpolation could lead to a more stable solution.

Bibliography

- ITTC (2002). 'ITTC – Recommended Procedures'. In: URL: <https://ittc.info/media/1365/75-04-02-01.pdf>.
- Jones, W.P and B.E Launder (1972). 'The prediction of laminarization with a two-equation model of turbulence'. In: *International Journal of Heat and Mass Transfer* 15.2, pp. 301–314. ISSN: 0017-9310. DOI: [https://doi.org/10.1016/0017-9310\(72\)90076-2](https://doi.org/10.1016/0017-9310(72)90076-2). URL: <http://www.sciencedirect.com/science/article/pii/0017931072900762>.
- Kim, Dong-Hwan (2020). *URANS V&V for KCS free running course keeping and maneuvering simulations in calm water and regular head/oblique waves*. eng.
- Leonard, B.P. (1979). 'A stable and accurate convective modelling procedure based on quadratic upstream interpolation'. In: *Computer Methods in Applied Mechanics and Engineering* 19.1, pp. 59–98. ISSN: 0045-7825. DOI: [https://doi.org/10.1016/0045-7825\(79\)90034-3](https://doi.org/10.1016/0045-7825(79)90034-3). URL: <http://www.sciencedirect.com/science/article/pii/0045782579900343>.
- Ngoc, Tu et al. (June 2019). 'Numerical Prediction of Propeller-Hull Interaction Characteristics Using RANS Method'. In: *Polish Maritime Research* 26, pp. 163–172. DOI: [10.2478/pomr-2019-0036](https://doi.org/10.2478/pomr-2019-0036).
- Prakash, Senthil and V. Subramanian (Sept. 2010). 'Simulation of Propeller - Hull Interaction Using Ranse Solver'. In: *The International Journal of Ocean and Climate Systems* 1, pp. 189–208. DOI: [10.1260/1759-3131.1.3-4.189](https://doi.org/10.1260/1759-3131.1.3-4.189).
- Przulj, V. and B. Basara (n.d.). 'Bounded convection schemes for unstructured grids'. In: *15th AIAA Computational Fluid Dynamics Conference*. DOI: [10.2514/6.2001-2593](https://doi.org/10.2514/6.2001-2593). eprint: <https://arc.aiaa.org/doi/pdf/10.2514/6.2001-2593>. URL: <https://arc.aiaa.org/doi/abs/10.2514/6.2001-2593>.
- Queutey, P. et al. (May 2017). 'Seakeeping Prediction of the ONRT Tumblehome in Head Waves with Unsteady RANS'. In: *VII International Conference on Computational Methods in Marine Engineering - MARINE 2017*. Nantes, France. URL: <https://hal.archives-ouvertes.fr/hal-02569791>.

- Queutey, Patrick and Michel Visonneau (2007). 'An interface capturing method for free-surface hydrodynamic flows'. In: *Computers & Fluids* 36.9, pp. 1481–1510. ISSN: 0045-7930. DOI: <https://doi.org/10.1016/j.compfluid.2006.11.007>. URL: <http://www.sciencedirect.com/science/article/pii/S0045793007000734>.
- Rhie, C. M. and W. L. Chow (1983). 'Numerical study of the turbulent flow past an airfoil with trailing edge separation'. In: *AIAA Journal* 21.11, pp. 1525–1532. DOI: [10.2514/3.8284](https://doi.org/10.2514/3.8284). eprint: <https://doi.org/10.2514/3.8284>. URL: <https://doi.org/10.2514/3.8284>.
- Salvesen, Nils (1978). 'Added Resistance of Ships in Waves'. In: *Journal of Hydronautics* 12.1, pp. 24–34. DOI: [10.2514/3.63110](https://doi.org/10.2514/3.63110). eprint: <https://doi.org/10.2514/3.63110>. URL: <https://doi.org/10.2514/3.63110>.
- Shen, Zhirong, Decheng Wan and Pablo M. Carrica (2015). 'Dynamic overset grids in OpenFOAM with application to KCS self-propulsion and maneuvering'. In: *Ocean Engineering* 108, pp. 287–306. ISSN: 0029-8018. DOI: <https://doi.org/10.1016/j.oceaneng.2015.07.035>. URL: <http://www.sciencedirect.com/science/article/pii/S0029801815003480>.
- Wang, Jianhua, Weiwen Zhao and De-Cheng Wan (Sept. 2016). 'Free Maneuvering Simulation of ONR Tumblehome Using Overset Grid Method in naoe-FOAM-SJTU Solver'. In:
- Wilcox, David C. (1988). 'Reassessment of the scale-determining equation for advanced turbulence models'. In: *AIAA Journal* 26.11, pp. 1299–1310. DOI: [10.2514/3.10041](https://doi.org/10.2514/3.10041). eprint: <https://doi.org/10.2514/3.10041>. URL: <https://doi.org/10.2514/3.10041>.